© 2017 Richard Dicky Liu

STRUCTURAL AND OPTICAL PROPERTIES OF PHASE TRANSITION CUBIC PHASE GALLIUM NITRIDE FOR PHOTONIC DEVICES

BY

RICHARD DICKY LIU

THESIS

Submitted in partial fulfillment of the requirements
for the degree of Master of Science in Electrical and Computer Engineering
in the Graduate College of the
University of Illinois at Urbana-Champaign, 2017

Urbana, Illinois

Adviser:

Assistant Professor Can Bayram

Abstract

Gallium nitride (GaN) semiconductors and its compounds (AlGaInN) have transformed the visible light emitting diode (LED) industry thanks to their direct bandgap across the entire visible spectrum and ultra violet. Despite its success, the conventional hexagonal-phase GaN has fundamental deficits that hinders performance. These include: internal polarization field (~MV/cm^2), high acceptor activation energy (260 meV), low hole mobility (20 cm^2/V), and expensive substrates (Al_2O_3, SiC). The metastable cubic-phase GaN offers interesting properties: no internal fields, lower acceptor energy (200 meV), and higher hole mobility (150 cm^2/V), that are preferable over the conventional hexagonal GaN through the higher symmetry in the cubic-phase crystal. Due its metastability, however, cubic GaN has not been synthesized with device-worthy crystal quality as large lattice mismatch between foreign substrates and relaxation to the hexagonal phase result in highly defective and mixed phase crystals. Therefore, the superior properties of cubic GaN could not be utilized.

This thesis explores the novel properties of cubic GaN grown on Si(100) via phase transition and nano patterning enabled through phase-transition modeling and cubic GaN material characterization. Crystal growth geometry of GaN in nano-patterned silicon U-shaped grooves separated by oxides are modeled through crystallographic equivalence to estimate the geometry of the structure and the required deposition height for complete cubic phase material transition. Structural characterizations, including scanning electron microscopy, electron backscatter diffraction, and transmission electron microscopy show excellent crystal uniformity and predictable phase transition behavior. Raman spectroscopy and cathodoluminescence show excellent phase purity and clearly controlled phase transition. Extensive optical characterization was conducted via polarization dependent photoluminescence and time-resolved photoluminescence to extract carrier recombination and photon emission behavior. Temperature-dependent cathodoluminescence was conducted to extract the Varshni coefficients for bandgap, defect luminescence activation energies, and most importantly the internal quantum efficiency.

To Monoclonal Antibody Conjugates

Acknowledgments

To begin, I must express my sincerest gratitude to my advisor, Professor Can Bayram, who has put the well-being and the success of my graduate career as the first priority through the inundating emails of recommendations, well-being checking-ups, friendly reminders, and ideas.

I would like to acknowledge my family, professors, colleagues, friends, and Claire for their never-ending support and encouragement. I would also like to acknowledge and thank Seattle Genetics, Inc. for Adcetris™ (Brentuximab Vedotin). My work here would not be possible without them.

I would like to acknowledge the support from Dr. James Mabon, Dr. Julio Soares, and Dr. Changqiang Chen of University of Illinois at Urbana-Champaign, IL, USA, and Dr. Richard Schaller of Argonne National Laboratory for sharing and teaching their expertise on conducting scientific research.

This work was supported by the National Science Foundation Faculty Early Career Development (CAREER) Program under award number NSF-ECCS-16-52871, and by the NASA Space Technology Research Fellowship (NSTRF17) under award number #80NSSC17K0150. Use of the Center for Nanoscale Materials, Argonne National Laboratory, an Office of Science user facility, is supported by the U. S. Department of Energy, Office of Science, Office of Basic Energy Sciences, under Contract No. DE-AC02-06CH11357. I also acknowledge the UIUC-MRL seed project #8016 for structural microanalysis.

Contents

CHAPTER 1 INTRODUCTION 1
1.1 Overview of Light Emitting Diodes 2
1.2 History of GaN 8
1.3 Overview of the Gallium Nitride Material System 9
1.4 Cubic Phase GaN and Its Metastability 13
1.5 Phase Transition Approach to c-GaN 16

CHAPTER 2 CRYSTALLOGRAPHY MODELING OF PHASE TRANSITION 20
2.1 Si(100) Substrate Patterning: U-Groove Fabrication 20
2.2 U-Groove Aspect Ratio Patterning Parameters Definition 23
2.3 Critical Patterning and Growth Condition for c-GaN Phase Transition 24

CHAPTER 3 STRUCTURAL PROPERTIES OF THE PHASE TRANSITION c-GaN 27
3.1 GaN Growth Dynamics and Modeling Verification 27
3.2 Cubic Phase Purity and Uniformity Verification 31

CHAPTER 4 OPTICAL PROPERTIES OF THE PHASE TRANSITION c-GaN 34
4.1 Room Temperature Light Emission Properties 34
4.2 Varshni Coefficient and Defect Luminescence 36
4.3 Quantum Efficiencies 47
4.4 Radiative Lifetime 48

CHAPTER 5 PHOTONICS OUTREACH ACTIVITIES 52
5.1 Intra-Institutional Educational Outreach 52
5.2 Inter-Institutional Outreach Activities 53

CHAPTER 6 CONCLUSION 54
6.1 Preliminary Research Findings 54
6.2 Future Work 54

REFERENCES 59

APPENDIX A INSTRUMENTS AND EQUIPMENT 65
A. 1 Scanning Electron Microscopy and Electron Backscatter Diffraction 65
A. 2 Atomic Force Microscopy 66
A. 3 Transmission Electron Microscopy 67
A. 4 Raman Spectroscopy 68
A. 5 Cathodoluminescence 69
A. 6 Photoluminescence 70
A. 7 Time-Resolved Photoluminescence 72

CHAPTER 1

INTRODUCTION

Photonics is the understanding, engineering, and technology of generating, manipulating, and detecting light waves and photons through electronics. It covers a broad range of wavelengths from radio waves to gamma rays and finds applications in consumer electronics, medicine, and space exploration. The amalgamation of our understanding of light and nanotechnology is poised to revolutionize how nano-photonics benefit our daily activities. From conventional (lighting) to emerging (therapeutic) applications, economic and technological demands have fueled the development of semiconductor-based lighting. The goal is to create energy-efficient, small footprint, inexpensive devices that can supplant the conventional solutions in energy (lighting, solar cells), consumer electronics (barcode scanners, blue-ray players), communications (data transfer), defense and national security (infrared camera, biological agent detection), health and medicine (Lasik, sanitation, disinfection), and manufacturing (laser cutting and machining). Innovation in nano-photonics will require improvement and incorporation of contemporary devices.

In this thesis, a novel approach to synthesize the superior photonic semiconductor material, the cubic phase gallium nitride, is pursued via modeling and extensive structural and optical characterization. The thesis is divided into six chapters as follows. Chapter 1 introduces the history and the operation physics of a light emitting diode. This is followed by a summary and overview of the material system contrasting the differences between hexagonal (h-) and cubic (c-) phase gallium nitride (GaN), and the conventional method of obtaining c-GaN and its disadvantage. Finally, the novel approach of this thesis to the synthesis of c-GaN is discussed. In Chapter 2, the growth dynamics and crystallographic modeling are presented to predict and estimate the condition for optimal c-GaN growth. In Chapter 3, structural analysis and phase purity investigation of the phase transition c-GaN are explored extensively to demonstrate the reliability

and quality of this new technology. In Chapter 4, optical properties of the material are studied to document the emission characteristics of the c-GaN obtained through this approach and to compare it against other methods to quantify the gain in performance. In Chapter 5, photonic outreach activities and accomplishments are outlined to show the broader impact of the work completed in this Master's thesis. In Chapter 6, a conclusion of the work accomplished and potential future research directions are presented.

1.1 Overview of Light Emitting Diodes

A light emitting diode (LED) is a two-terminal electrical device that emits light via electroluminescence when a forward electrical current is applied. An illustrative schematic is shown in Figure 1 (right). The device, similar to a regular rectifying diode, is consist of a P-doped region (dark gray) and an N-doped region (light gray) that together forms a p-n junction.

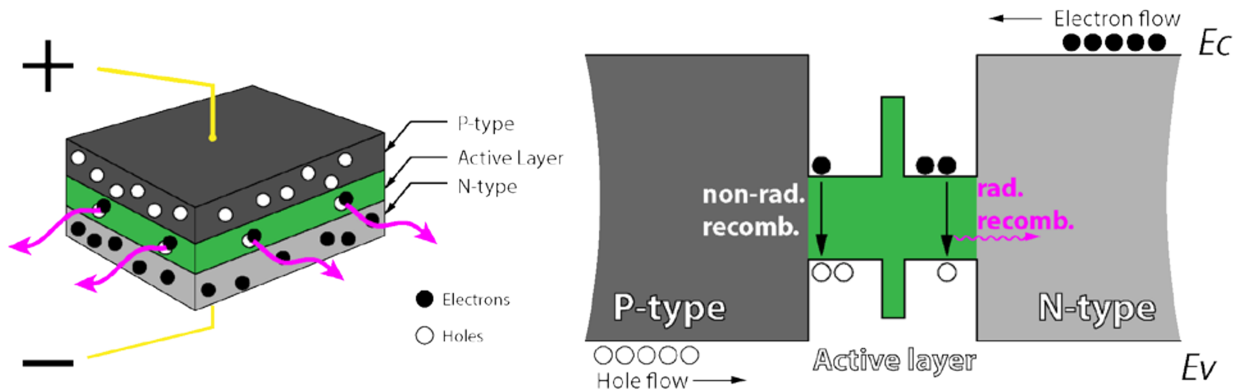

Figure 1 (Left) Schematic of an LED, (right) Energy diagram of the LED.

The injection of holes (white dots) from the positive terminal and electrons (black dots) from the negative terminals causes the carriers to recombine in the active layer (green), and if the material has a direct bandgap, a photon is emitted (purple). The active layer, which is situated in the depletion region of the p-n diode, is usually composed of multiple stacks of quantum wells and barriers. The photon emitted from this region is dictated by the material properties (bandgap, recombination rate, recombination mechanism) and the confinement energies. An illustration of the energy diagram of the LED is shown in Figure 1 (left). The holes and electrons from the P- and N-type regions, respectively, are confined by the

active region and undergo either radiative recombination to emit a photon or non-radiative recombination to emit heat in the form of lattice vibration called phonons.

In the III-V semiconductor family, which is composed of elements from column three (Al, Ga, In) and elements from column five (N, P, As, Sb), an array of compound semiconductors can form. Depending on the combination of the elements, the resulting binary semiconductor can have bandgap energies range from 0.35 eV (InAs) to 6 eV (AlN) with either a direct or indirect bandgap. The combination of two of the elements from either group III or V and one element from the other group forms a ternary alloy. It will have a bandgap energy that is a combination (with bowing) of the bandgap energies of the underlying binary semiconductor. A graph summarizing the bandgap energies and lattice constants of the common III-V semiconductors are shown in Figure 2. The visible range of photon energies are highlighted by the rainbow to demonstrate the corresponding color.

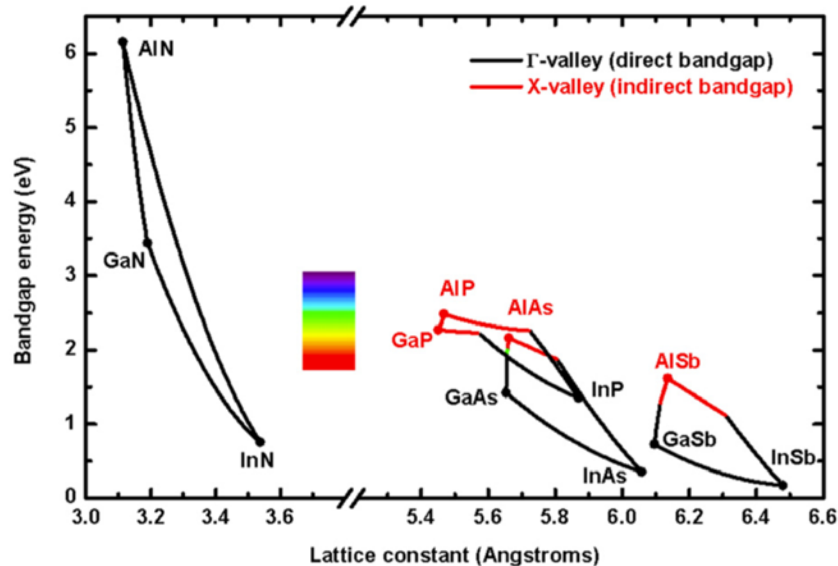

Figure 2 Bandgap energies of common III-V semiconductors. Reprinted from D. Zhu, *et al.*, Rep. Prog. Phys. 76, 106501 (2013), with the permission of AIP Publishing.

To make a visible emitter, a semiconductor with bandgap energy in the visible range (400~700 nm or 1.77~3.1 eV) is required. In the III-V family, this leads to III-nitrides (full vis-spectrum coverage), and III-arsenides and III-phosphides (yellow-red only). This makes the III-nitrides, and particularly GaN, of

great interest, as alloying with a small fraction of In can form an emitter that covers the entire visible range, which would enable full-spectrum solid-state lighting.

The first LED was invented by James Biard and Gary Pittman at Texas Instrument in 1961 with GaAs emitting in the infrared (900 nm).[1] Their LED was based on a semi-insulating GaAs substrate and uses a simple p-n junction to facilitate the radiative recombination. In 1962, the first visible LED (and laser diode) was demonstrated by Professor Nick Holonyak using $GaAs_{1-x}P_x$ emitting in the red (700 nm) at General Electric.[2] In 1972, George Craford, an University of Illinois doctoral graduate, improved the brightness of the red LED by a factor of ten and invented the first yellow LED.[3] The GaAsP based LEDs enabled the implementation commercialization of solid-state lighting to replace the conventional sources such as incandescent and neon lamps in indicators (e.g. seven-segment digit displays). On the other side of the visible spectrum, the first high-brightness blue LED was demonstrated by Shuji Nakamura, Isamu Akasaki and Hiroshi Amano in 1994 using $In_xGa_{1-x}N$.[4] With the advent of the blue LED, the generation of white light became possible most commonly through either down-conversion of blue light to yellow by the cerium doped yttrium aluminum garnet (Ce:YAG) yellow phosphor approach (B+Y) or through the mixing of red, green and blue LEDs approach (RGB).

Since its invention, the B+Y white LED has transformed the general lighting industry, providing a light source that is capable of an electrical luminescence efficacy of 190+ lm/W (theoretical limit ~ 300 for white LED with color rendering index >90), surpassing the most efficient conventional light source, the sodium vapor lamps, with the added benefits such as: better color rendition, longer lifetime, robustness, etc. The three inventors of the blue LED were awarded the 2014 Nobel Prize in Physics for their discovery of the blue LED and the successful p-doping of III-nitride semiconductors. This approach to white lighting, however successful, is less than ideal. The yellow phosphor introduces Stokes losses as the blue photons are being converted to yellow photons despite the very high quantum yield (>97%).[5] This represents an inherent loss (~20%) that cannot be mitigated. Additionally, the yellow phosphor experiences thermal quenching[6] and low chemical stability that reduces the efficiency of down conversion

and luminescence intensity as the device ages. The lack of emission in the red (>650 nm) from the phosphor makes the color rendering (CRI ~70-80) of this approach to general lighting less than ideal as the light produced often seems too harsh and lacks in warmth compare to sunlight. To overcome this, red phosphor, such as europium-based phosphor, is added to the yellow phosphor. However, this type of phosphor is typically less efficient as it introduces additional Stokes losses, and its thermal quenching is more severe. Most importantly, the emission spectrum of these phosphor white LEDs is not tunable, as there is essentially only a blue LED with passive phosphor coating that is always active. This necessitates the use of thin-film transistor filters in displays that use the white LED as their backlight has to filter out unwanted colors. The disadvantage of this type of backlighting is the poor contrast between pure white and pure black, and the loss of efficiency to heat when the unwanted photons are blocked. These disadvantages of the B+Y white LEDs have fueled the research for the phosphor-free full spectrum RGB LEDs.

Although efficient blue and red emitters with quantum efficiency (QE) of >70% are readily available, green emitters are not, creating the so-called “green gap”.[7] The comparison between the quantum efficiencies of LEDs emitting in the red (650 nm) to UV-C (200 nm) is shown in Figure 3.

The causes of the green gap are different for the phosphide and nitride families. The bandgap of III-phosphides turns indirect as the aluminum composition increases (to reduce the wavelength from red → green);[8] this makes the phosphide unsuitable for light emission, whereas the crystal quality of the III-nitrides suffers as the composition of indium increases (to increase the wavelength from UV → green) caused by a phenomenon called indium clustering.[9] Together, the two semiconductor families form a sharp drop in the QE around 570 nm.

The performance of the blue LED is at the very root of the efficiency of the blue + phosphorus white LEDs until a suitable green LED is found for the RGB white LEDs. The efficiency of a III–nitride blue LED under various injection current is shown in Figure 4. Under low injection current density (<10A/cm^2) and therefore the low power operation regime, blue LEDs exhibit excellent overall efficiency of >75%, as

shown in Figure 3. However, under high-power operation with high injection current density (10 A/cm^2), the quantum efficiency of the LEDs drops significantly.

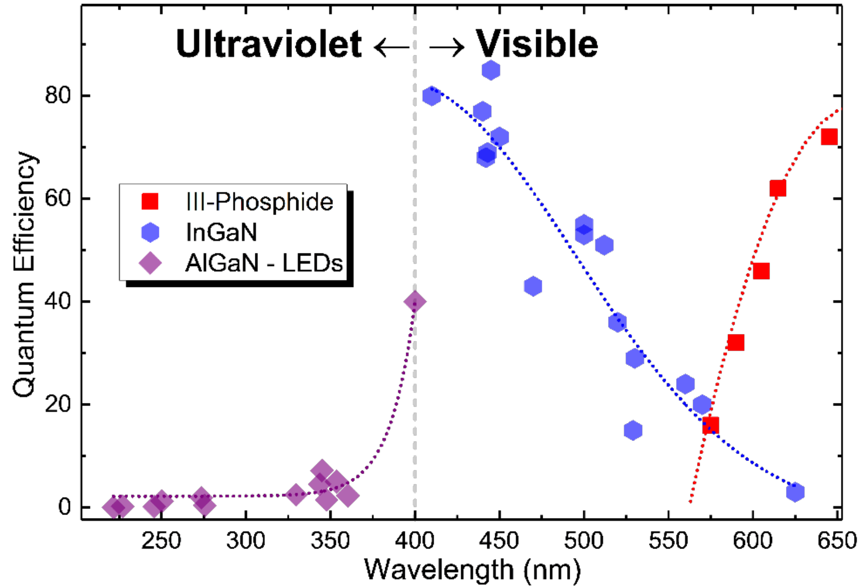

Figure 3 External quantum efficiencies of nitride and phosphide LEDs showing a lack of efficient emitter in the "green gap". Plotted with data provided in (Auf Der Maur *et al.*, 2016)[7] and (Zhang *et al.*, 2016)[10]

This phenomenon, "efficiency droop", limits the exploitation of the InGaN-based LEDs.[11,12] Studies have proposed the many origins of efficiency droop including: poor hole injection,[13] carrier overflow,[14,15] polarization,[16] Auger recombination,[17] carrier delocalization,[18] high defect density,[19] etc. However, researchers have not reached a consensus, and droop-free LEDs have not yet been demonstrated.[20] In order to have more light output, more and/or larger LEDs are required to maintain a level of efficiency, therefore the upfront equipment cost and device footprint increase as the consequences. The use of phosphor in the white LEDs also induces loss of efficiency and aging effects under prolonged operation at elevated temperature. This is a major bottleneck to the widespread adoption of LED for general lighting purposes, as the upfront cost is often prohibitively high, making solid-state lighting only economically feasible with capricious subsidies offered by the manufacturer or government.

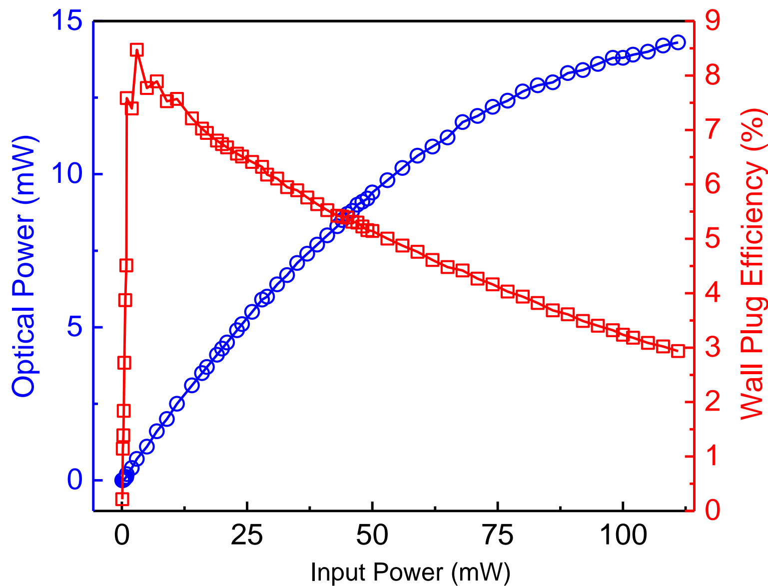

Figure 4 Efficiency droop of the blue III-nitride LED at various forward current.

On the other side of the spectrum in the ultraviolet (UV) range, solid-state lighting has remained relatively unexplored. Ultraviolet radiation has many uses including: surface disinfection, water sanitation, and biological agent detection (e.g. anthrax), among others. The conventional sources of UV light are discharge lamps with vapor constituents of mercury (Hg) or xenon bromide (XeBr) – which are both toxic. Additionally, these UV light sources have short lifetimes, are fragile, have a large footprint, and require a warm-up time (2–15 min), and degrade with on/off cycles. Their emission spectrum depends on the vapor selection (e.g. mercury or other halogens) and thus cannot be tuned to target specific microbes. In addition to these technological limitations, there is significant equipment and operational (i.e. energy) cost associated with these gas-discharge lamps. LEDs offer a solution to overcome these disadvantages of the Hg lamp with its small footprint, ability to work off the grid, and mechanical robustness, and reliability. Unfortunately, the state-of-the-art AlGaN-based UV LEDs are not an attractive alternative due to their even poorer efficiency, as seen in Figure 3, where deep UV (<300 nm) LEDs often exhibit QE less than 1%. The unsatisfying performance of UV-LED makes it unable to replace conventional UV sources despite the

aforementioned advantages of LEDs. This inefficiency limits not only the practicality of AlGaN-based LEDs, but also laser diodes (LDs). Hence, AlGaN related UV research is of high importance and technology

Ultraviolet (UV) lasers have shown important applications in space technology, such as laser interferometer space antenna (LISA) for gravitational wave observation, light detection and ranging (LIDAR, Lidar in-space technology experiment (LITE) and Lidar Atmospheric Sensing Experiment (LASE)) for planetary atmospheric measurements (e.g. "dust devils" on Mars), and chemical spectroscopy for toxic gases, etc. Conventional UV laser sources such as: the gas lasers (XeF, He-Cd, XeCl, ArF), and the solid-state lasers (Nd:YAG (3rd and 4th harmonics), frequency tripled Ti:Sapphire) either have a very large form factor, requires external pumping, are very inefficient (requires frequency up-conversion), and/or are difficult to modulate. On the other hand, semiconductor lasers and laser diodes (LDs) offer extremely compact (<1 cm in length), inexpensive and simple designs that can achieve high power, high efficiency, high gain, high modulation speed, high monochromaticity, and excellent reliability and longevity. LDs in the infrared ~ red range have already been commercialized, and have changed the capability of long distance communication to handheld presenters. Lasing with InGaN at 405 nm has been commercialized with success, but lasing in the deeper part of the UV spectrum (<355 nm) using AlGaN has not been realized with satisfying results. The goal of improving the performance of InGaN for the green LEDs, and AlGaN for the UV LEDs and LDs makes the study of the GaN material essential for the next-generation photonics.

1.2 History of GaN

Gallium nitride was first successfully synthesized by reacting gallium tribromide with dry ammonia gas ammonia in 1932.[21] The gallium ammonate synthesized resembles the chemical properties of indium and aluminum ammonate. The first synthesis of single crystalline GaN was reported in 1969 on c-plane sapphire single-crystalline substrates prepared by vapor-phase growth with Ga-halide and ammonia.[22] Its properties including: direct bandgap (3.39 eV), lattice constants, coefficient of thermal expansion, chemical stability (water, acid and base insolubility) etc., were reported. A very high electron concentration ($>10^{19}$ cm^{-2}) was

observed due to the high concentration of nitrogen vacancy. However, the inability of this early research to grow high-quality crystals and to P-dope the material limited the usefulness of GaN.

In 1986, crack-free GaN was grown on sapphire by using an AlN nucleation layer and metalorganic chemical vapor deposition (MOCVD).[23] The AlN layer mitigates the large lattice mismatch (–13.8%) between GaN and sapphire, and the optimized MOCVD growth greatly reduced the density of vacancies. The P-doping challenge was overcome when Mg-doped GaN was treated with low-energy electron-beam irradiation, which activates the Mg dopants.[24] The Mg-activation was also demonstrated by simple thermal annealing at 700 °C in N_2-ambient in 1992; and it achieved a hole concentration of 3×10^{17} cm^{-3}.[25] The researchers' discovery of hydrogen passivation of Mg dopants led to the successfully fabrication of high-efficiency blue LED, which led to the 2014 Nobel Prize.

1.3 Overview of the Gallium Nitride Material System

GaN is a wide bandgap semiconductor that thermodynamically crystalizes in the hexagonal (wurtzite) phase (h-GaN), although under the correct environment and circumstance it can also form in the cubic (zinc blende) phase (c-GaN). With other group III elements, GaN can theoretically form alloys with Al and In to form AlGaInN that covers the UV-C to infrared range of the optical spectrum (6.0 ~ 0.68 eV). Selected material properties are shown in Table 1. A ball and stick model of h-GaN is shown in Figure 5.

Table 1 Select material properties of III-nitride materials.

	E_g (eV) at 300 K	Lattice Constant *a* (Å)	Lattice Constant *c* (Å)
h-GaN[27]	3.42	3.189	5.185
h-AlN[27]	6.0	3.112	4.982
h-InN[27,28]	0.68	3.545	5.703
c-GaN[29,30]	3.22	4.5	-
c-AlN[27,31]	5.3*	4.38	-
c-InN[27,32]	0.60	4.98	-

***indirect bandgap**

Due to its crystal stability, GaN photonics and other devices are conventionally fabricated on the (0001) c-plane of the thermodynamically stable hexagonal (wurtzite) material phase on substrates such as Al_2O_3,[33] 6H-SiC,[34] and Si(111) with innovative buffer layers.[35]

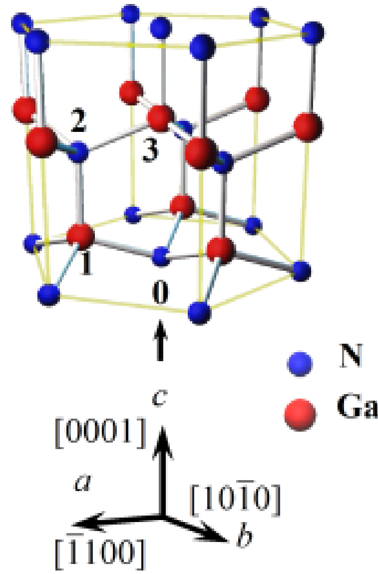

Figure 5 Atomic arrangement of h-GaN crystal. Figure is taken from the website of Matsuoka Laboratory, Tohoku University.[26]

The wurtzite crystal structure inherently lacks inversion symmetry in the (0001) direction, and as a result, spontaneous and, when strained, piezoelectric polarization fields are generated.[36] The polarization fields push the electrons and holes towards the opposite direction along the c-axis. This phenomenon, quantum confined Stark effect (QCSE), reduces the wave function overlap between the carriers in the active regions of a multiple quantum well (MQW) LED structure, and consequently the radiative recombination rate is also reduced, as shown in Figure 6.[37] Under high injection level, the excessively high concentration of carriers in the opposite sides of the active layer induces Auger recombination, which is the promotion of an electron in the conduction band to a higher level by the energy released by a nearby electron-hole recombination. This three-particle process has a third-order dependence on the carrier density and rapidly becomes more prominent in LEDs under a high injection regime.[17]

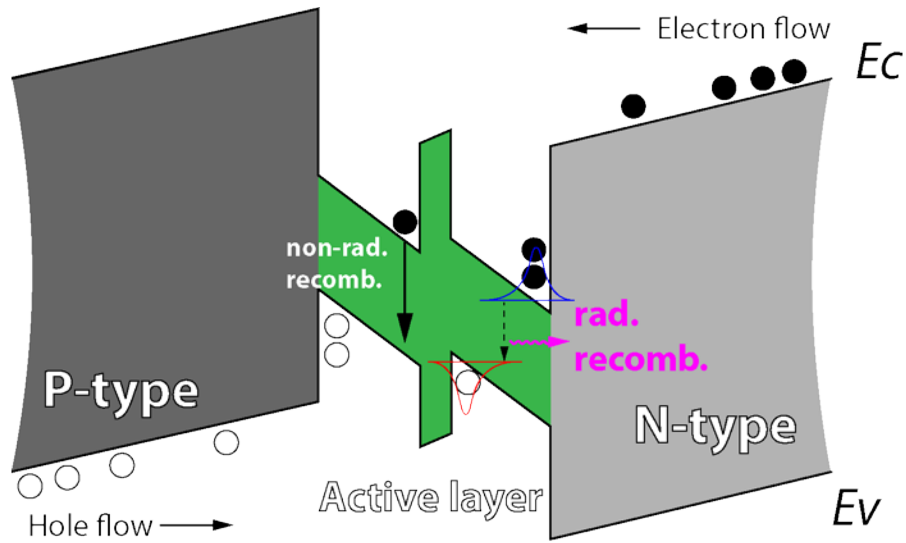

Figure 6 LED energy diagram under polarization fields.

Other detrimental properties that are inherent to the h-GaN crystals also limit the effectiveness and the potential of photonic devices fabricated on this material. The low p-doping efficiency, due to the large activation energy of Mg (260 meV), necessitates a very high doping concentration to achieve a practical hole concentration; this in turn increases impurity scattering, which is undesirable as it reduces the carrier mobility and increases the ohmic loss of the material. The large difference in carrier mobility causes the electrons to overshoot and the holes to undershoot the active layer, causing uncontrolled recombination to happen outside the active layer. This would result in either the emission of photons in the UV range or phonons, which are heat losses. The measures to mitigate the electron overshoot (more wells) leads to the exacerbation of poor hole injection into the quantum well, and vice versa. The larger bandgap in h-GaN means that a higher Indium composition is needed to create an InGaN active layer with a suitable bandgap to emit in the green part (~555 nm) of the spectrum. The high indium content causes inhomogeneity in the active layer, which creates local minima in the energy bands. Increasing current density causes these minima to become saturated and the carriers to spill over to the low indium region, which emits in a short wavelength. Higher indium content also induces a stronger piezoelectric field, which further aggravates the detrimental effect of QCSE. An PL spectrum of a InGaN/GaN LED is shown in Figure 7.

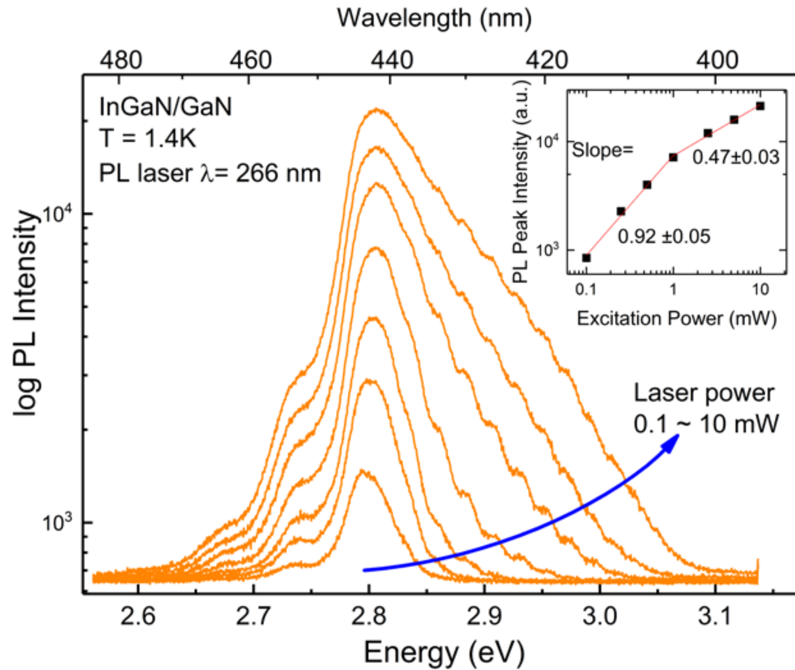

Figure 7 PL spectrum of a InGaN/GaN blue LED showing the emergence of a "blue shoulder" at higher injection level. The inset shows the intensity of the 2.8 eV peak intensity as a function of laser power.

Under high laser power (>1 mW), a shoulder appears on the high energy (or the blue side) of the main peak at 2.8 eV. At this level, carriers are being spilled-over from the local energy minima to emit higher photons. Saturation of these minima can be seen through the drastic reduction in the marginal intensity gain of the 2.8 eV peak, as shown in the inset. Additionally, h-GaN lacks ideal natural cleaving planes that could act as the mirrors of the Fabry-Perot cavity for laser applications. The quality factor of the laser cavity obtained from using h-GaN is therefore low, causing the threshold current to increase to offset the losses.

To overcome some of these effects, other h-GaN crystal facets, such as the non-polar m-plane $(1\bar{1}00)$, a-plane $(\bar{1}\bar{1}20)$, as shown in Figure 8, have also been explored for polarization-free semiconductor devices. However, these substrates suffer from low availability, small and impractically expensive substrates, lack of scalability and poor material quality. [38,39]

These material characteristics of h-GaN makes it a challenging semiconductor to fabricate devices on as special considerations need to be taken. These measures are sometimes mutually exclusive

(polarization-free vs crystal quality) or simply do not exist (efficient P-dopants, high hole conductivity). However, its closely related material, the c-GaN, offers many desirable properties that promises to overcome the challenges h-GaN faces.

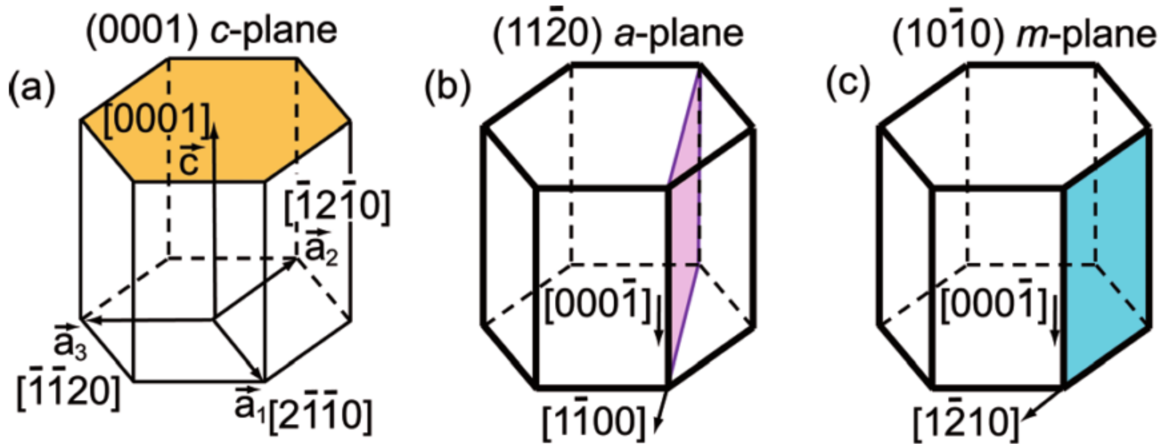

Figure 8 Planes of h-GaN. (a) the conventional polar (0001) c-plane, and the non-polar (b) $(11\bar{2}0)$ and (b) $(10\bar{1}0)$ planes of the hexagonal crystals. Reprinted from A.E. Romanov *et al.*, J. Appl. Phys. 109, (2011), with the permission of AIP Publishing.

1.4 Cubic Phase GaN and Its Metastability

With the crystal structure with higher symmetry, cubic (zinc-blende) phase GaN (c-GaN) is inherently polarization-free in the growth direction <100>, and literature has shown these fields to be absent in c-GaN.[40] The crystal structure of the c-GaN is shown in Figure 9.

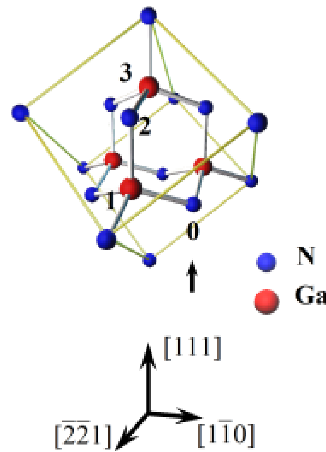

Figure 9 Atomic arrangement of c-GaN crystal. Figure is taken from the website of Matsuoka Laboratory, Tohoku University.[26]

Additional to its polarization-free nature, c-GaN has properties beneficial for photonic applications. The higher symmetry of the crystal results in a low carrier scattering rate.[41] This means a higher hole mobility and conductivity,[42] and a higher electron drift velocity.[43] The hole mobility has been reported to be more than ten times as large as its h-GaN counterpart (20 vs. 350 cm^2/Vs).[44] The absence of internal polarization fields in the material growth direction allows for a more even carrier distribution, which leads to a greater wavefunction overlap in the active layer that results in a fast radiative recombination. This prevents the build-up of a high concentration of carriers that leads to Auger recombination.[45] Additionally, the population inversion in the active layer is also enhanced, which leads to a much higher optical gain observed in c-GaN.[46] The availability of cleavage planes in the cubic crystal permits the creation of atomic flat edges, which can be used as the high reflectivity cavity mirrors of an edge emitting Fabry-Perot laser. Due to its weak spin-orbital coupling, very long room-temperature electron-spin relaxation lifetime has been observed in c-GaN. Selected material properties are tabulated in Table 2 to compare the two material phases.

Table 2 Comparison of selected material properties of h- and c-GaN.

	h-GaN	c-GaN	Advantage of c-GaN
E_g (eV)[29]	3.42	3.22	Less indium for green
μ_n (cm^2/Vs)[47]	1000	1000	Higher injection symmetry
μ_p (cm^2/Vs)[47]	30	350	
$E_{acceptor}$ (meV)[48]	260	215	Higher doping efficiency
Polarization (MV/cm)[40,49]	3.5	0	Greater wavefunction overlap
Drift velocity (10^7 cm/s)[43] @ 100kV/cm	2.2	3.4	Switching speed
Optical gain (cm^{-1})[50] @ 15E18 cm^{-3}, TE	1500	4000	Lower lasing threshold
Cleaving plane	No (Al_2O_3)	Yes (Si)	Laser cavity

The smaller bandgap (E_g = 3.22 eV) of c-GaN necessitates a smaller (–10%) indium composition to emit at wavelengths in the green in comparison to h-GaN, which has bandgap energy that is slightly, but not insignificantly, larger (E_g = 3.42 eV).[51] Literature has shown microcrystals of c-GaN to have a smaller

level efficiency droop, and exhibits output power that is 50% stronger than its h-GaN counterpart.[52] These reported properties make the c-GaN fundamentally a superior photonic semiconductor than h-GaN, and a promising material for improving the performance of contemporary photonic devices. [53]

Besides polarization-free photonics, other polarization-free wide bandgap applications of c-GaN ranging from, normally-off transistors,[54] room-temperature ferromagnetism,[55] high-temperature spintronics,[56] and single photon emitters.[57] Yet, c-GaN is one of the least studied materials due to its phase instability and its tendency to relax to the thermodynamically stable h-GaN.

Researchers at the turn of the 21st century have put forth their effort in pursuit of the superior properties of the c-GaN. However, its phase metastability on conventional planar substrates (GaAs,[58] 3C-SiC,[49] Si(100),[59] and MgO,[60] or via impurity incorporation)[47,61] has prohibited the synthesis of high-quality materials. GaN grown via the planar heteroepitaxy approach often results in highly defective and mixed phase material, as crystals relax to form the more stable h-GaN.[62,63]

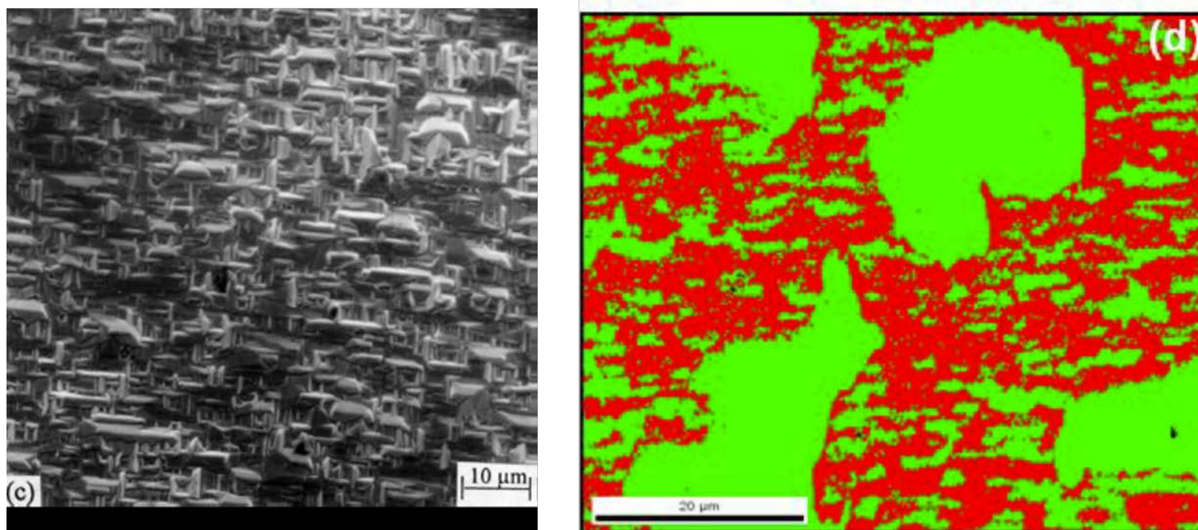

Figure 10 (Left) SEM image of MOCVD growth of c-GaN on 3C-SiC.[59] Reprinted from C.H. Wei, *et al.*, J. Electron. Mater. 29, 317 (2000), with the permission of Wiley Publishing. (Right) Phase distribution of MBE grown GaN on 3C-SiC showing cubic (red) and hexagonal (green) phases. Reprinted from R.M. Kemper, *et al.*, J. Cryst. Growth 323, 84 (2011), with the permission of Wiley Publishing.

Figure 10 (left) shows a scanning electron microscopy (SEM) image of a MOCVD grown c-GaN on 3C-SiC, which has the smallest lattice mismatch. A very rough surface with ridges growing in perpendicular

directions are observed. On the right, electron backscatter diffraction (EBSD) crystal phase detection of molecular beam epitaxy grown GaN on GaAs, which also has cubic crystal structure, shows c-GaN (red) regions with h-GaN (green) mixture, while the large h-GaN regions is phase pure and free of c-GaN inclusion. This demonstrates how c-GaN relaxes to h-GaN, but not vice versa. Neither of these approaches result in a epilayer that is adequate for device fabrication. As such, there exists a need for a more reliable approach for fabricating c-GaN.

1.5 Phase Transition Approach to c-GaN

The difficulty and the unsatisfying outcome of growing c-GaN on planar substrates initiated alternative methods to the material. The most promising alternative approach to synthesizing c-GaN is through the hexagonal-to-cubic phase transition. Due to crystal plane equivalence of the cubic (111) and the hexagonal (0001) planes, h-GaN and h-AlN will nucleate on the (111) planes of cubic substrates. Indeed, LEDs based on the conventional h-GaN can be fabricated on Si(111) wafers, albeit with a poorer performance than its sapphire equivalent due to the worse crystal quality as a result of a larger lattice mismatch. Instead of using a Si(111) wafer, the (111) planes can be exposed on a Si(100) wafer using the anisotropic KOH etching technique. Aqueous KOH solution with isopropanol alcohol will preferentially attack the Si(100) plane at a rate that is approximately 900 times more quickly than that of Si(111) planes.[64] The result is the formation of V-shaped grooves with the (111) planes on the either sides that make a 54.7° angle to the substrate. Using standard photolithography techniques, periods of SiO_2 can be deposit on top of the Si(100) wafer to act as a protective hard mask for the KOH etching. Predefined periods of V-grooves can then be etched onto the wafer. The resulting patterned Si(100) substrate is shown in Figure 11.

During MOCVD growth, h-GaN will selective nucleate on the exposed Si{111} planes, resulting in the growth of two h-GaN "wings" that are angled 109.47° with respect to each other. Studies have shown that when two h-GaN coalesce at the tetrahedron bonding angle, which coincides with the angle provided by the geometry of the V-groove, the GaN crystal will relax to the cubic phase.[65] A single period V-groove

demonstrating the crystal geometry of the hexagonal-to-cubic phase transition is shown in Figure 12. The phase transitioned c-GaN (blue) plateau is flanked by two h-GaN (red) wings that are buried underneath.

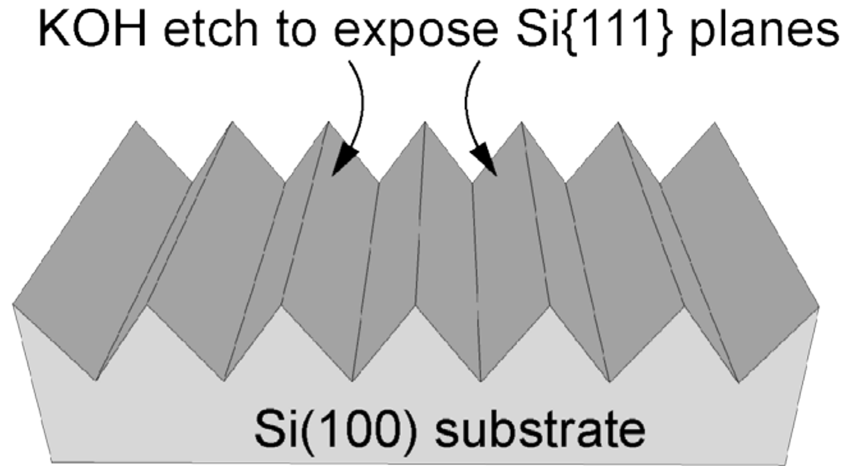

Figure 11 V-groove patterned Si(100) substrate.

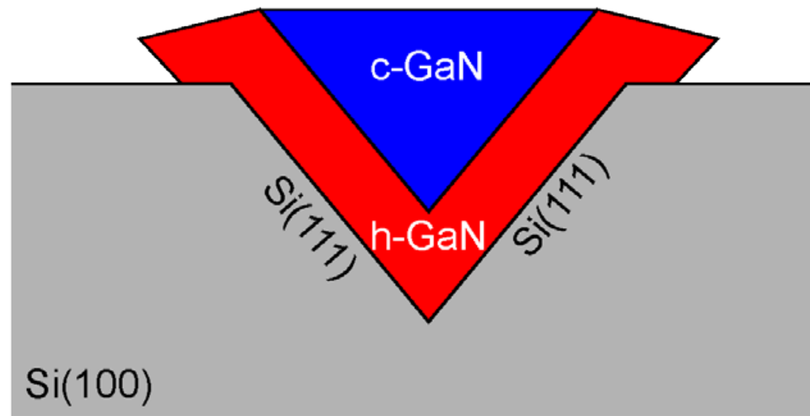

Figure 12 A single period V-groove.

This approach has shown excellent phase purity and crystal quality as no phase mixing is observed in either, but distinct wings of h-GaN that have not undergone phase transition are still present on the surface.[66] Employing multiple periods of the V-groove on a substrate results in the h-GaN wings penetrating through neighboring c-GaN plateaus, as shown in Figure 13. The inability of the V-groove approach to suppress the h-GaN wings necessitate remedies in order to make the phase transition c-GaN usable for device fabrication.

A refined approach to the phase transition method is through the U-shaped grooves (U-groove) instead of the V-grooves on the same Si(100) substrates using MOCVD.[67] Using KOH anisotropic wet etching of Si on substrate patterned with SiO_2, U-shaped grooves with a SiO_2 – Si(111) – Si(100) – Si(111) – SiO_2 surfaces are created. Barriers made of dielectrics, such as SiO_2, placed between each period suppresses the growth of the unwanted h-GaN. With the correct patterning and growth parameters, the c-GaN can cover the h-GaN wings completely. The result is a purely cubic surface, as shown in Figure 14.

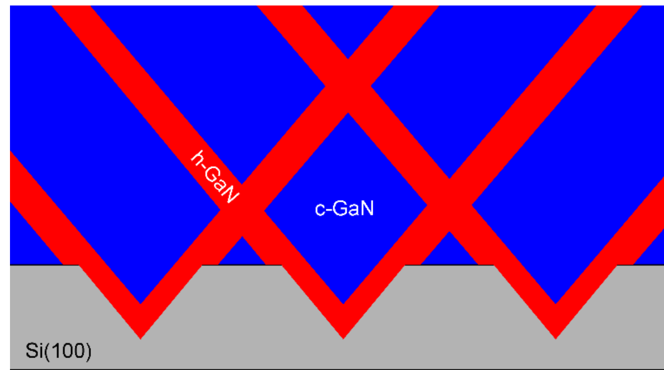

Figure 13 Multiple V-grooves showing periodic h-GaN mixing.

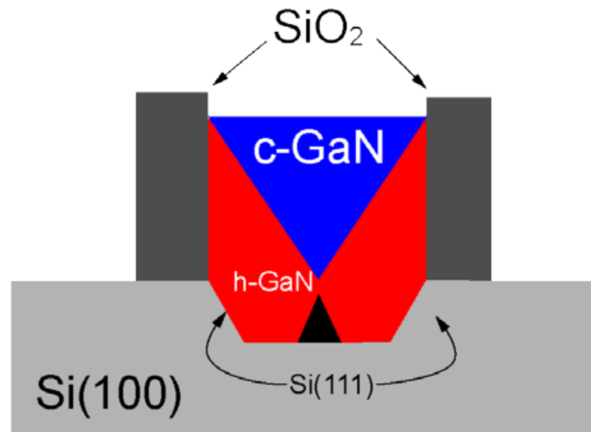

Figure 14 The U-groove approach to c-GaN can achieve complete c-GaN surface coverage under critical patterning and growth conditions.

With its ability to form a surface composed of entire c-GaN, the U-groove approach to phase transition and c-GaN photonics seems promising. The use of on-axis, 750 μm thick and 200 mm diameter Si(100) as the substrate makes this approach to inexpensive, compatible with existing large-scale fabrication techniques, and able to integrate with silicon logic and photonic devices. The material is poised

to have a big impact on the semiconductor industry, and therefore is worthy of extensive research in order to fully capitalize the superior properties of c-GaN.

The following chapters are dedicated to the optimization of this technology. Chapter 2 describes the crystallography modeling of the growth of GaN in the U-groove and the critical condition for complete c-GaN surface coverage. In Chapter 3, structural investigations with the aim to verify the crystal modeling, and to characterize the structural and phase uniformity. In Chapter 4, optical properties, such as temperature dependence, defect centers, radiative lifetime, and efficiencies of the phase transition c-GaN are addressed. Chapter 5 briefly outlines the outreach activities engaged during this Master's degree. Chapter 6 then concludes the thesis and sets a future plan to pursue a doctoral degree.

CHAPTER 2

CRYSTALLOGRAPHY MODELING OF PHASE TRANSITION

Given the non-planar nature of the U-grooves, the growth dynamics and crystal geometry must be taken into consideration to enable a well-optimized growth structure to enable complete c-GaN on the surface without phase mixing. The first section describes the growth dynamics of the two phases of GaN. The second section describes the various physical dimensions of the U-groove. The third and last sections focus on the derivation of the critical condition for full c-GaN coverage.

2.1 Si(100) Substrate Patterning: U-Groove Fabrication

Based on crystallographic geometry that h-crystal <0001> and c-crystal <111> directions are equivalent, it has been shown if two h-phase <0001> growth fronts merge at an angle of ~110° (i.e. the angle between the two Ga-N bonds in the tetrahedral bonding), c-phase would form after the seam, as shown in Figure 15.

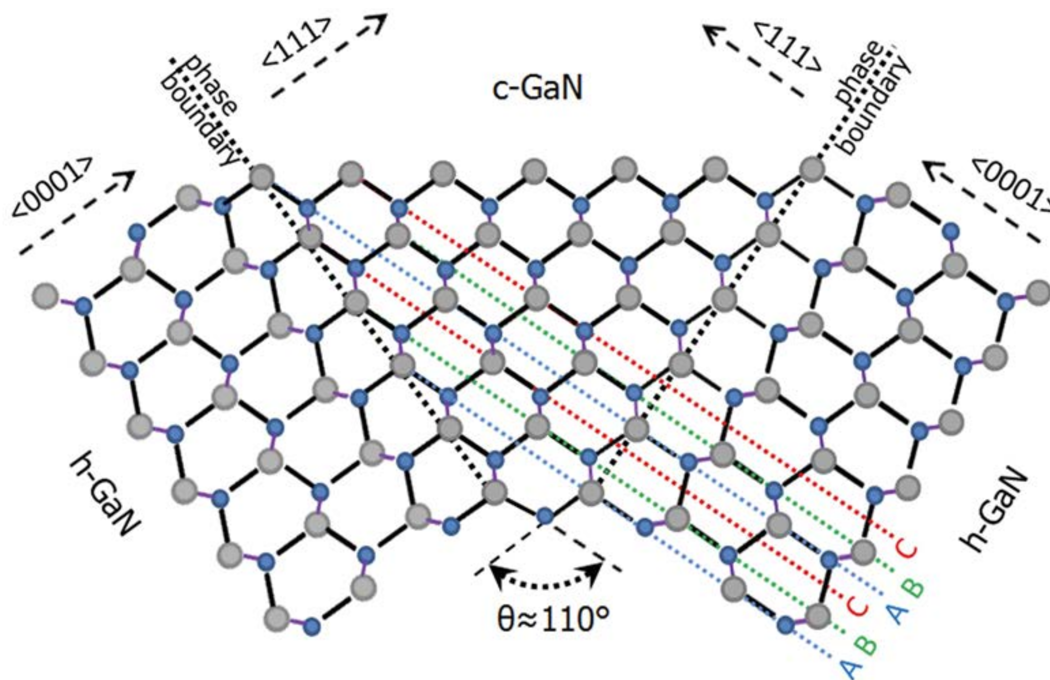

Figure 15 Cross-sectional sketch depicting wurtzite to cubic phase transition observed in the groove. Reprinted from C. Bayram *et al.*, Adv. Funct. Mater. 24, 4492 (2014), with the permission of Wiley Publishing.

Anisotropic nano-patterning of Si(100) substrates are typically used to create U-shaped (or V-shaped if etched all the way) grooves with a crystallographic angle of 54.74° between the (100) and (111) Si surfaces. Thus, GaN selective MOCVD-growth on Si(111) facets of a U-groove leads to two h-GaN growth fronts meeting at an angle of $54.74° \times 2 \approx 109.47°$, which is exactly the angle required to facilitate the transition of the h- GaN into c-GaN after coalescence. The material growth process is shown in Figure 16.

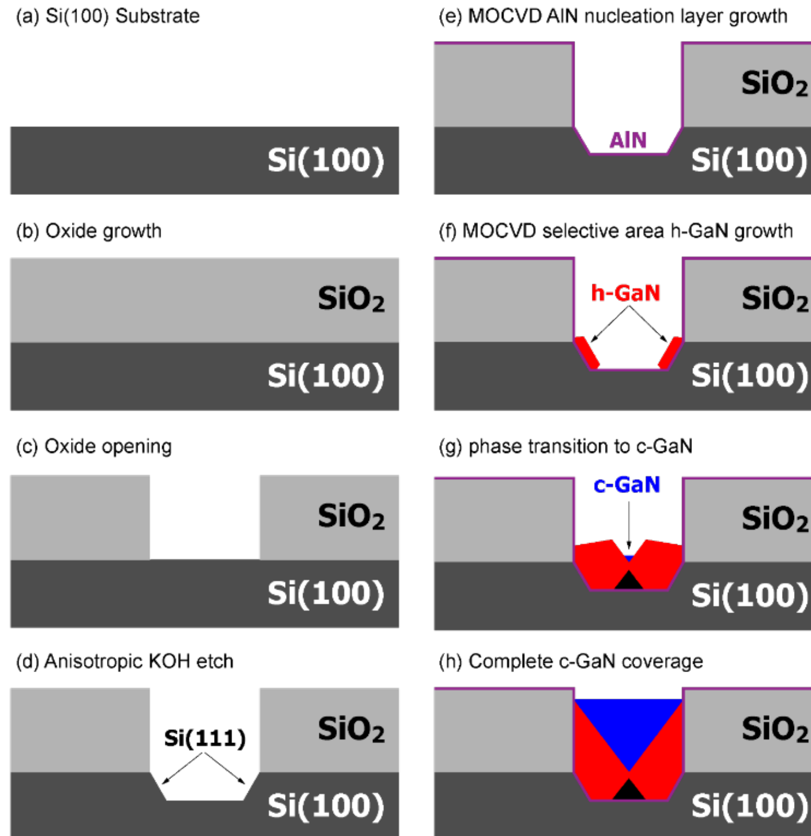

Figure 16 Schematic figures of the substrate preparation and material growth. (a) On-axis 200 mm Si(100) substrates are used. (b) Thermal oxide is grown on the substrate. (c) The oxide is etched away to create a groove. (d) KOH anisotropically etches the exposed Si, creating two opposing Si(111) planes. (e) An AlN nucleation layer is deposited everywhere via MOCVD. (f) h-GaN is selectively grown on the Si(111) planes at 54.7° to the substrate. (g) When the two h-GaN "wings" coalescence, the material is phase transitioned to c-GaN. (h) Further MOCVD growth allows the c-GaN to cover the entire surface.

Figure 16 shows the substrate preparation and the growth pattern of GaN. An on-axis (a) Si(100) substrate is used to maximize scalability and compatibility. A layer of (b) thermal oxide is grown on the substrate, then (c) openings are formed using dry etching techniques. The substrate is then etched with KOH to form (d) U-shaped grooves with two opposing Si(111) planes. The patterned substrate then undergoes

MOCVD III-nitride growth. A thin (~17 nm) AlN nucleation layer is deposited (e) on the surface to mitigate the large lattice mismatch between GaN and Si(111). Since the (111) plane of the cubic crystal is equivalent to the (001) plane of the hexagonal crystal, h-GaN will selectively nucleate on the (f) opposing Si(111) planes. After an adequate amount of h-GaN growth, the two opposing wings will coalesce in the (g) middle of the groove. This forces the GaN to phase transition to the cubic phase to incorporate the additional symmetry imposed by the h-GaN wings. The c-GaN will grow preferentially and stably until the (h) entire surface is composed of purely c-GaN. A 3D schematic of the phase-transition in progress is shown in Figure 17 (a), and the corresponding false-colored SEM image is shown in (c). The ideal case, where complete c-GaN coverage is achieved, is shown as (b) 3D schematic and (d) SEM image.

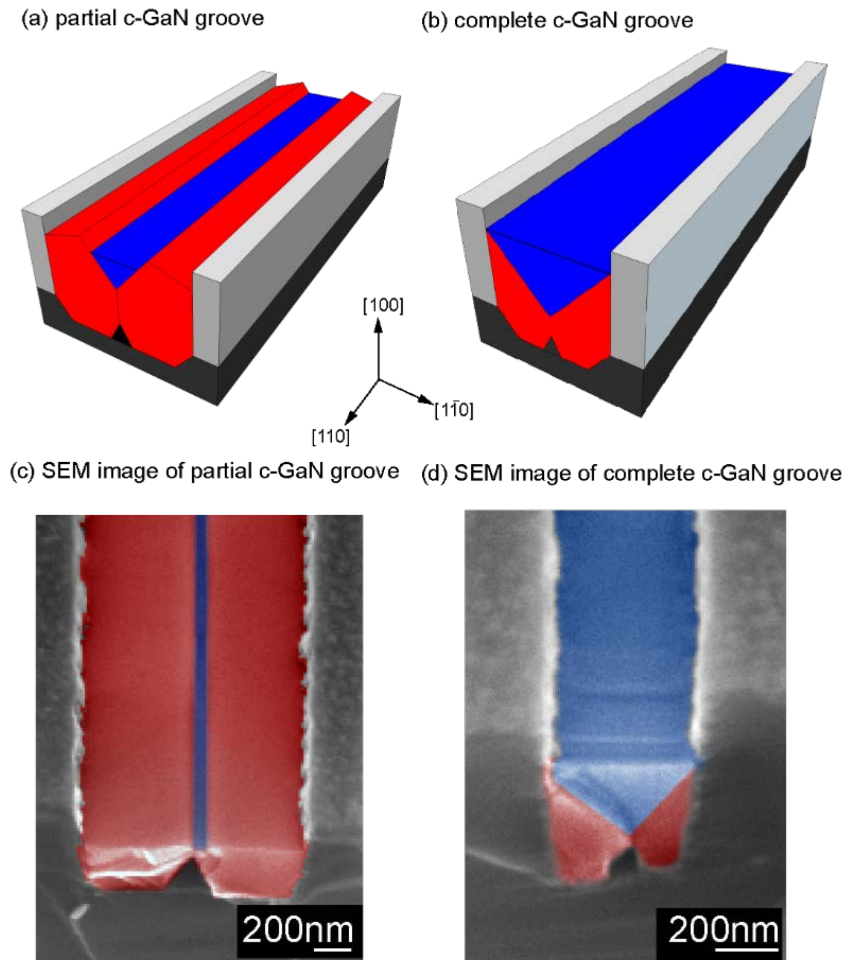

Figure 17 3D schematics of the U-grooves at (a) partial coverage and (b) complete coverage of c-GaN. Their corresponding false-colored SEM images are shown in (c) partial and (d) complete c-GaN coverage. Blue = c-GaN and red = h-GaN.

2.2 U-Groove Aspect Ratio Patterning Parameters Definition

Figure 18 shows the model sketch of GaN in a U-groove. The V- shaped red dashed lines refer to the phase boundaries where hexagonal-to-cubic phase transitions occurs,[67] and the top (red) dashed line indicates the c-GaN top surface. Under the selective growth conditions,[68] GaN nucleates on the Si(111) facets only and these h-GaN growth fronts meet at a 109.48° angle in the middle of the groove. After the middle of the growth fronts meet (point A in both figures), GaN grown on top will phase transition to cubic phase. Under these experimental / crystallographic observations, the geometrical modeling is carried out.

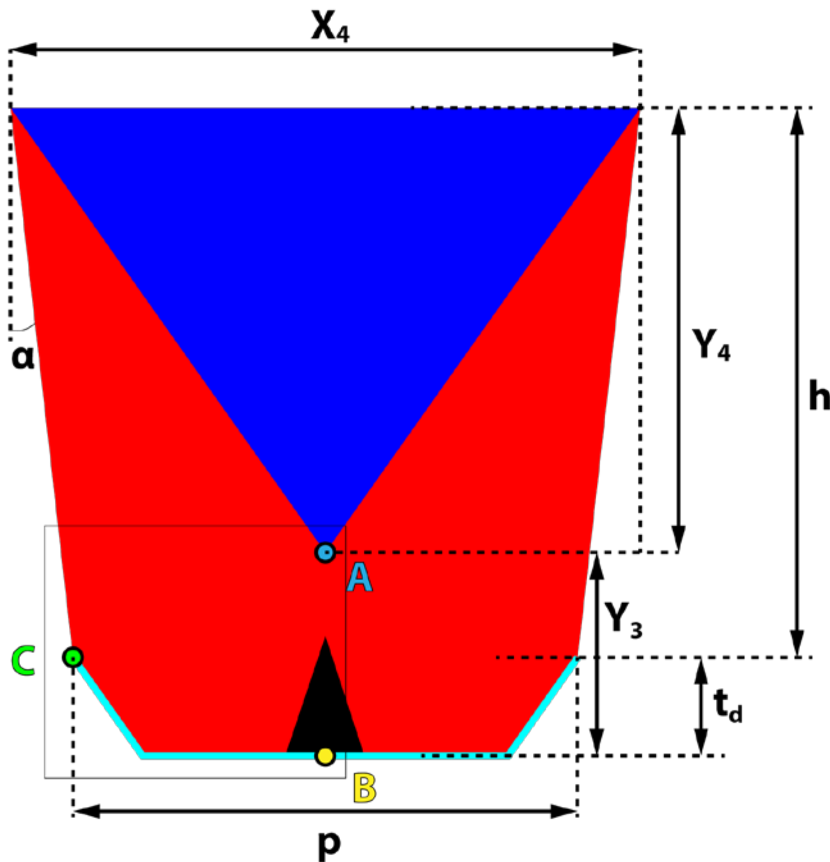

Figure 18 U-groove model and patterning parameter definition. Blue = c-GaN, red = h-GaN.

Figure 19 shows the zoomed-in region indicated by the dotted square in Figure 18. Points A, B, C in both figures (Figure 18, Figure 19) correspond to the same exact locations. The crystallographic angles (54.74° between the (100) and (111) Si surfaces) are shown accordingly.

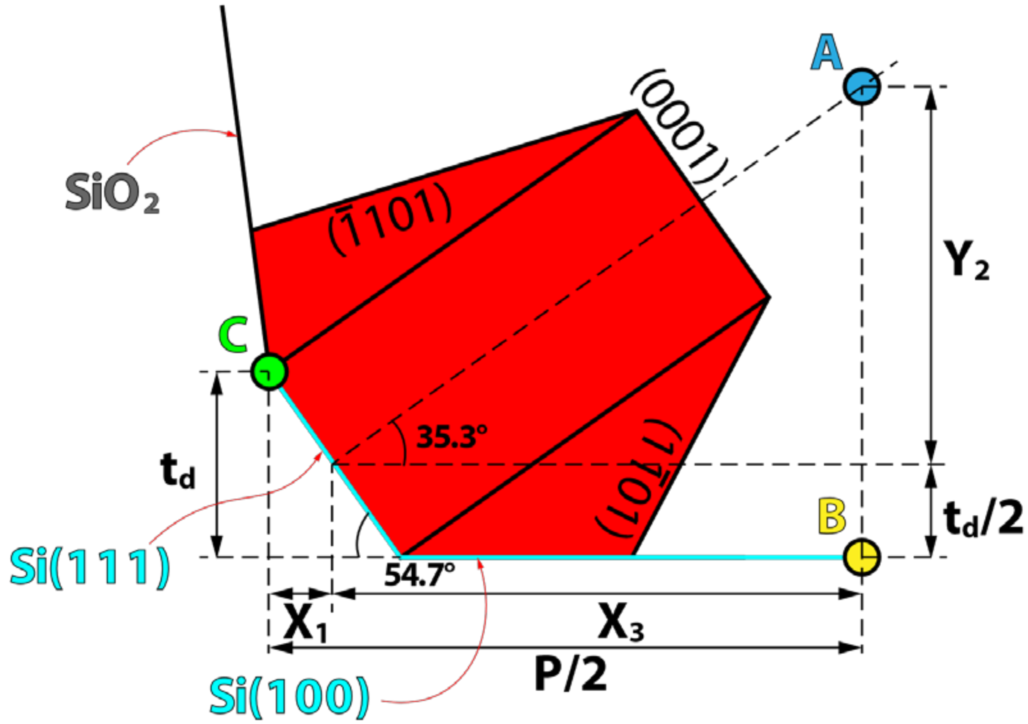

Figure 19 Selective area growth of h-GaN in U-groove.

2.3 Critical Patterning and Growth Condition for c-GaN Phase Transition

In the following derivation x_i and y_i are various dimensions as shown in the Figure 18 and Figure 19, h_c is the critical GaN deposition thickness (defined as the GaN deposition height above Si(100) that maximizes cubic phase GaN coverage on the U-groove surface), t_d is the etch depth, p is the opening width, and α is the oxide sidewall angle.

From Figure 19, we see that:

$$tan35.3° = \frac{y_2}{x_3} \tag{2.1}$$

$$tan54.7° = \frac{t_d}{2x_1} \tag{2.2}$$

$$x_1 + x_3 = \frac{p}{2} \tag{2.3}$$

$$y_3 = y_2 + \frac{t_d}{2} \tag{2.4}$$

Rearranging (2.1), (2.2), and (2.3), we get:

$$y_2 = x_3 tan35.3° \tag{2.5}$$

$$x_1 = \frac{t_d}{2tan54.7°} \tag{2.6}$$

$$x_3 = \frac{p}{2} - x_1 \tag{2.7}$$

Substituting (2.6) into (2.7):

$$x_3 = \frac{p}{2} - x_1 = \frac{p}{2} - \frac{t_d}{2tan54.7°} \tag{2.8}$$

Then using (2.8) in (2.5):

$$y_2 = x_3 tan35.3° = \left(\frac{p}{2} - \frac{t_d}{2tan54.7°}\right) tan35.3° \tag{2.9}$$

From Figure 18,

$$x_4 = p + 2\, h_C\, tan\, \alpha \tag{2.10}$$

$$y_1 + y_3 = h_C + t_d \tag{2.11}$$

$$tan35.3° = \frac{x_4}{2y_1} \tag{2.12}$$

Rearranging (2.12) using (2.10), and (2.11) using (2.4):

$$y_1 = \frac{x_4}{2tan35.3°} = \frac{p + 2\, h_C\, tan\, \alpha}{2tan35.3°} \tag{2.13}$$

$$h = y_1 + y_3 - t_d = y_1 + y_2 - \frac{t_d}{2} \tag{2.14}$$

Substituting (2.13) and (2.9) in (2.14), we get:

$$h_C = \frac{p + 2\, h_C\, tan\, \alpha}{2tan35.3°} + \left(\frac{p}{2} - \frac{t_d}{2tan54.7°}\right) tan35.3° - \frac{t_d}{2} \tag{2.15}$$

Solving for h_c:

$$h_C = \left(1 - \frac{tan\alpha}{tan\, 35.3°}\right)^{-1} \left[\left(\frac{p}{2} - \frac{t_d}{2tan\, 54.7°}\right) tan\, 35.3° + \frac{p}{2tan35.3°} - \frac{t_d}{2}\right] \tag{2.16}$$

Simplifying and plugging in values for the tangents, the relationship between critical thickness and the patterning parameters can be simplified. To achieve the complete c-GaN coverage condition, the U-groove parameters: oxide opening width (p), silicon etch depth (t_d), dielectric sidewall angle (α), deposition thickness (h) of GaN deposited above the Si(100) substrate surface has to obey:[69,70]

$$h = \left(1.06p - 0.75t_d\right) / \left(1 - \tan\alpha / 0.71\right) \quad (2.17)$$

CHAPTER 3

STRUCTURAL PROPERTIES OF THE PHASE TRANSITION c-GaN

In this chapter, structural characterization of the phase transition cubic phase GaN will be described. The first section will discuss the structural analysis of the nano-groove using scanning electron microscopy. The second section will cover the characterization of the phase transition using electron backscatter diffraction phase detection, Raman spectroscopy, and cathodoluminescence.

3.1 GaN Growth Dynamics and Modeling Verification

Based on our proposed crystallographic geometry modeling, a schematic of the growth pattern of GaN in a U-groove seen from the side is shown Figure 20a. For complete c-GaN surface coverage in these U-grooves, the critical GaN deposition thickness (h_c) is shown obeying Equation (2.17), where p is the opening width of the U-groove at the dielectric/substrate interface, t_d is the silicon etch depth, and α is the dielectric sidewall angle (Figure 20a). Additionally, we define a quantity, fill factor (*ff*) as $ff = h/h_c$, to quantify the ratio between actual and ideal GaN deposition thickness for complete c-GaN surface coverage. Here h is defined as the GaN deposition thickness above the Si(100) substrate level (Figure 20 (b), 20 (c), 20 (d)).

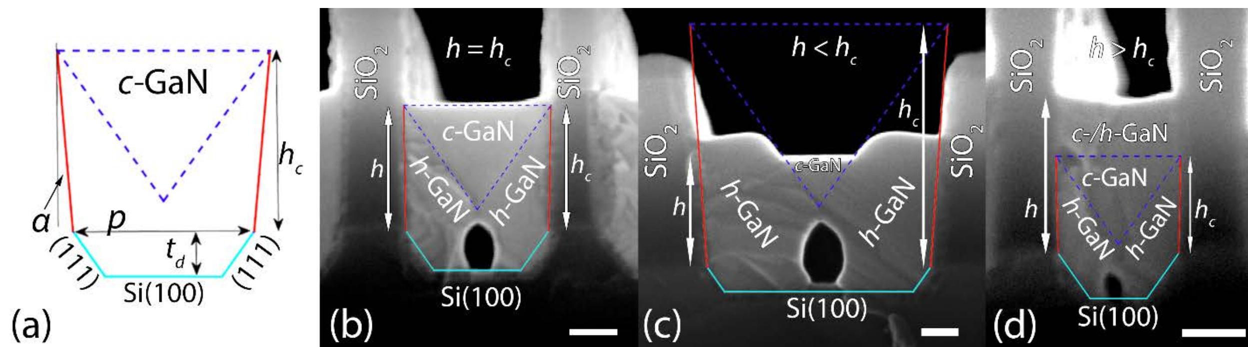

Figure 20 (a) Schematic defining critical deposition thickness (h_c), etch depth (t_d), opening width (p), and sidewall angle (α). Cross-sectional SEM views of GaN deposited in a U-groove when: (b) ($h \approx h_c$) Complete c-GaN surface coverage is achieved (*ff* ≈ 95%) (c) ($h < h_c$) the U-groove is under-filled with GaN (*ff* ≈ 40%). (d) ($h > h_c$) The U-groove is over-filled with GaN (*ff* ≈ 120%). This leads to phase-mixing. The white scale bars in the bottom right of each figure correspond to 100 nm. Reprinted from R. Liu and C. Bayram, Appl. Phys. Lett. 109, 38 (2016), with the permission of AIP Publishing.

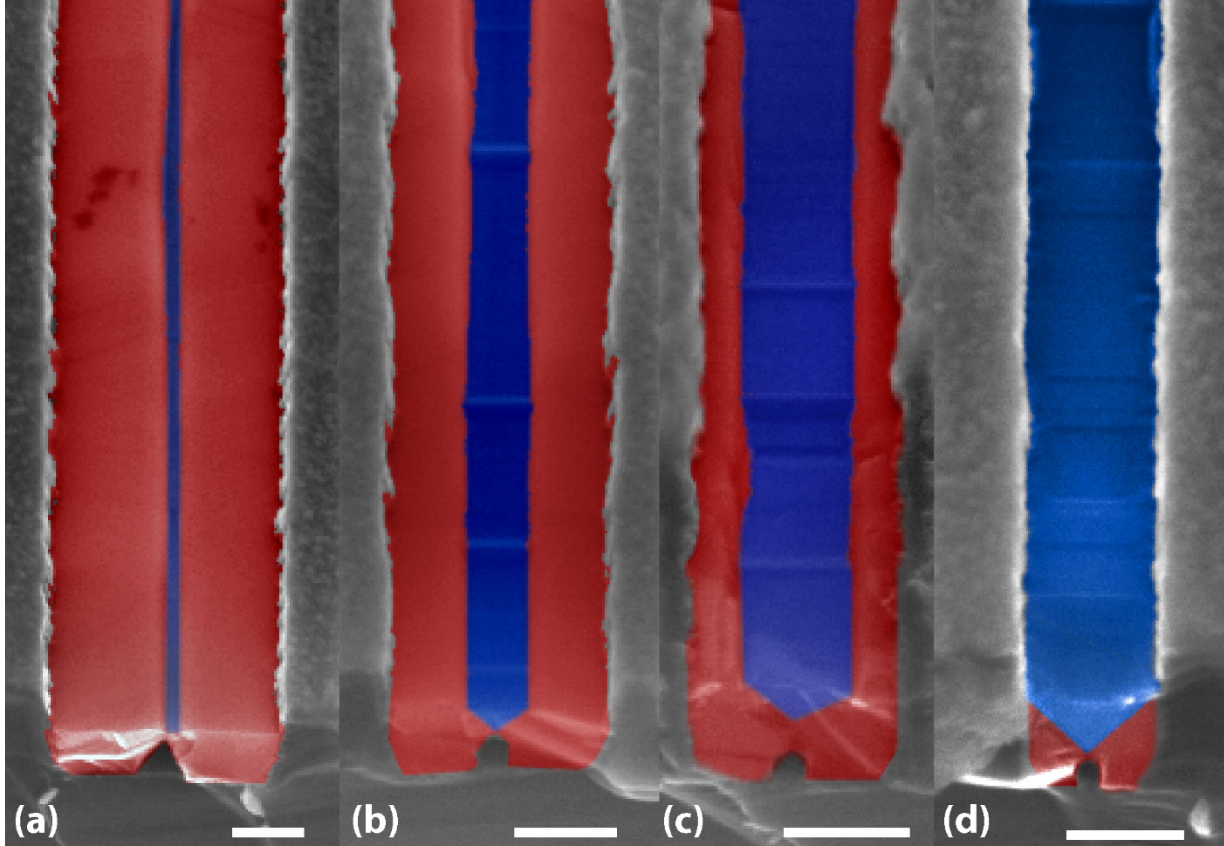

Figure 21 False-colored 45° SEM view of the U-grooves with *ff* of (a) 30%, (b) 45%, (c) 70%, (d) 95%. Blue = c-GaN, red= h-GaN. Scale bars all indicate 350 nm.

SEM study was conducted on JEOL 7000F Schottky field emission scanning electron microscope. Figure 20 (b), 20 (c), 20 (d) show cross-sectional scanning electron microscope (SEM) images of GaN in three different U-grooves. Figure 20 (b) is close to an ideal case (*ff* ≈ 95%) where GaN has a perfect fill ($h \approx h_c$) for the patterning parameters of t_d = 80 nm, p = 300 nm; and $\alpha \approx 2°$. The top c-GaN(100) surface is seen very flat. Figure 20 (c) shows an under-filled case ($h < h_c$, *ff* ≈ 45%) with t_d = 70 nm, p = 640 nm; and $\alpha \approx 4°$. On the surface, a small amount of the flat c-GaN(100) can be seen in the center flanked by two h-GaN $(1\bar{1}01)$ planes, which make a 7° angle to the (100) planes of both the Si substrate and c-GaN. For c-GaN to cover the entire surface, more deposition is needed. Figure 20d shows an over-filled case ($h > h_c$, *ff* ≈ 170%) in which too much GaN has been deposited for t_d = 70 nm, p = 190 nm; and $\alpha \approx 1°$. There is no identifiable crystal plane on the surface, implying over-deposition of GaN ($h > h_c$) causes the over-filled GaN to phase mix and lose its crystallinity.

Figure 21 shows the false-colored 45° plane-view SEM view of *ff* = (a) 30%, (b) 45%, (c) 70% and (d) 95% U-grooves with blue and red indicating c-GaN and h-GaN, respectively. The progression of c-GaN growth is clear, uniform and predictable. As *ff* approaches 100%, the blue c-GaN plateau covers an increasing amount of surface area to eventually the entirety of it, as seen in Figure 21 (d).

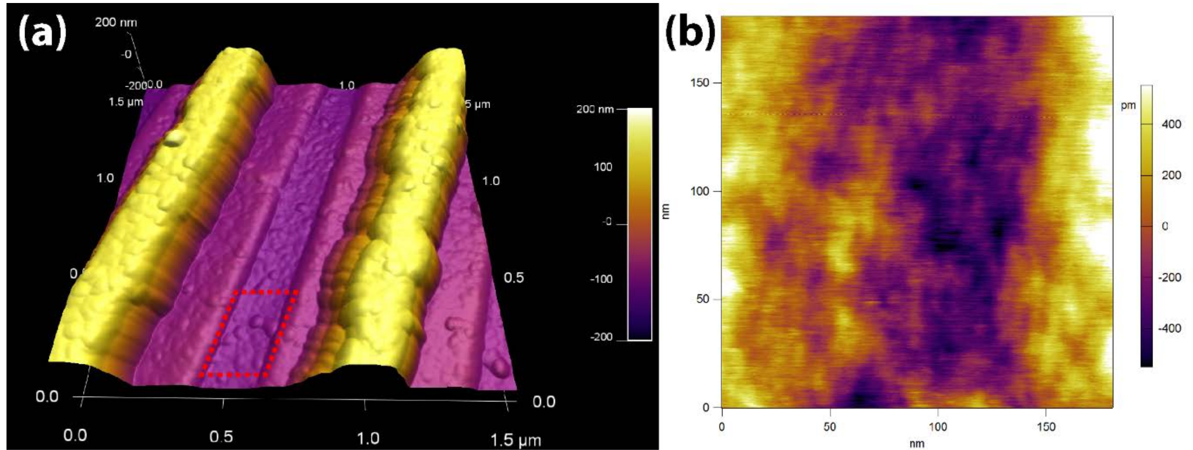

Figure 22 (a) 3D rendering of the *ff* = 45% U-groove. (b) AFM image of the marked c-GaN region.

Atomic force microscopy (AFM) can examine the surface morphology of the semiconductor to study the crystal growth dynamics and defectivity. Figure 22(a) shows the 3D rendering of the *ff* = 45% U-grooves, which have incomplete c-GaN surface coverage. The c-GaN can be seen sandwiched between two h-GaN wings, which themselves are confined by two taller oxide barriers. Figure 22 (b) shows the AFM image of the dotted area in 22 (a). The root-mean-square roughness of the c-GaN region is calculated to be 2.65 Å, which shows a high-quality and device-ready surface.

Transmission electron microscopy (TEM) study is conducted to characterize the crystal quality of the GaN materials in a U-groove, as shown in Figure 23 (a) bright field and (b) dark field images. The zone axis $\left[1\bar{2}10\right]$ of the dark field image is shown as a white vector *g*, which corresponds to (0002). A highly defective thin (~15 nm) layer of AlN is seen covering the Si substrate and the amorphous oxide barriers. Near the h-GaN nucleation sites on the Si(111) planes, both TEM images show crystals containing dislocations and stacking faults. The h-GaN crystals that are more than 50 nm away from the nucleation cites show increased quality, and dislocations are rarely observed. A ~20 nm long seam oriented

perpendicular to the substrate is observed in the middle of the groove between the two-opposing h-GaN wings directly above the void. It terminates into two distinctly straight interfaces extending toward the oxide sidewalls to form distinct V-shaped boundary. Enclosed in the V-boundary is the c-GaN cubic crystal which is further confirmed by TEM electron diffraction taken from the triangular area shown in Figure 18.

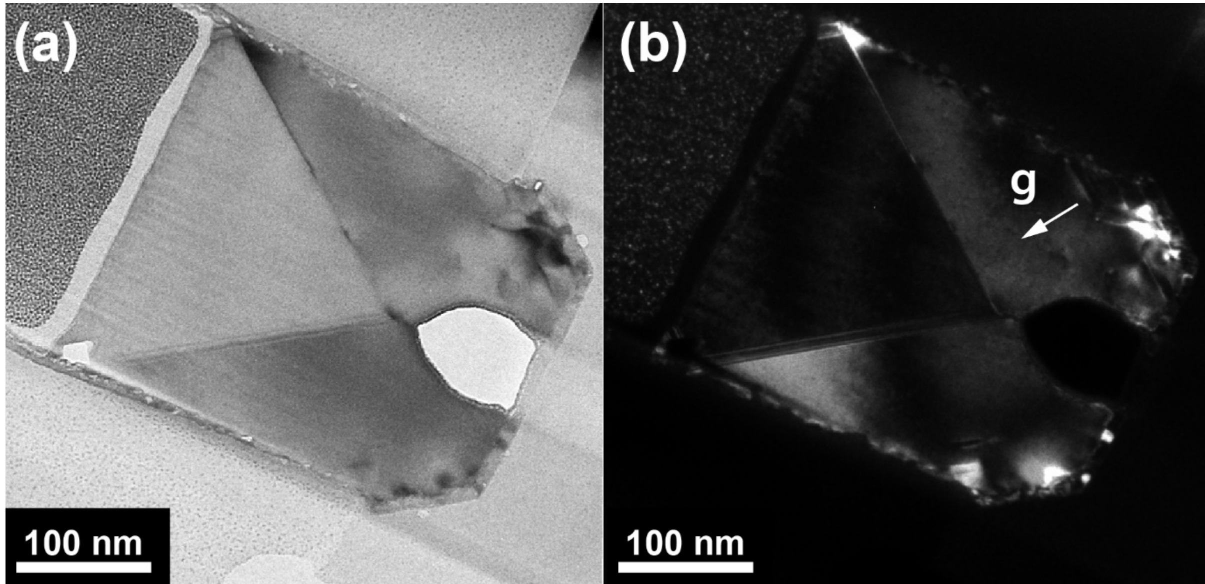

Figure 23 TEM images of GaN crystals in a U-groove. (a) bright field and (b) dark field image taken at g = (0002) near the $[1\bar{2}10]$ zone axis of the right-side h-GaN.[71]

Stacking faults parallel to the interface, i.e., lying on the c-GaN (111) and h-GaN (0001) planes are observed to accommodate the transition between the two crystal structures, but are limited to within in a few layers of atoms thick (not shown). At the c-GaN/oxide interface near the surface, defects (stacking faults) are observed to orient away from oxide (Figure 23b). Defective and mixed-phase material are observed above these stacking faults and the aforementioned critical height, *hc*. This demonstrates the importance of silicon substrate patterning and GaN growth optimization, as inadvertent relaxation of c-GaN to mixed-phase material can occur at the c-GaN/barrier.

3.2 Cubic Phase Purity and Uniformity Verification

Further electron backscatter diffraction (EBSD) measurements are carried out in order to study the distribution and location of the different GaN phases on U-groove the surfaces. Phase detection was conducted on the same JEOL 7000F fitted with a HKL Technology EBSD System with a high-resolution EBSD camera for crystallographic measurements, high-speed texture mapping, and phase identification. Analysis was done with HKL's Channel 5 Tango software.

Using a beam current of 2 nA and acceleration voltage of 15 kV, the EBSD setup can sample the very top layer (~10 nm) of the sample. This depth is calculated via Monte Carlo simulation taking that the electrons contribute to the EBSD patterns should lose very little energy (<100 eV) since the Kikuchi bands formed are discrete and distinct.

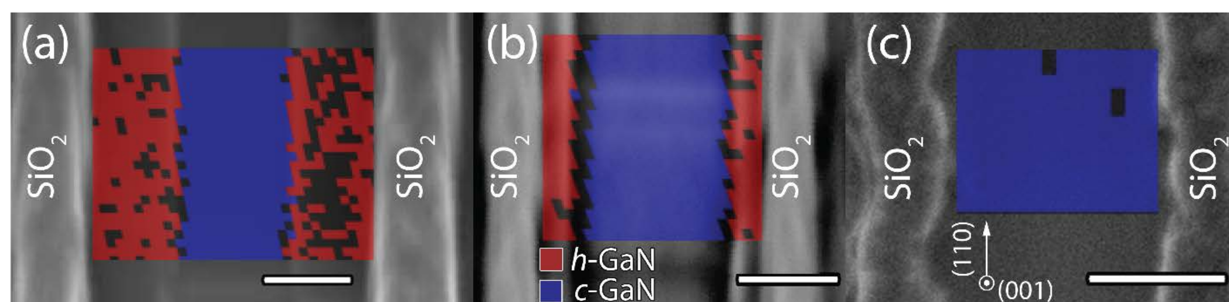

Figure 24 Top-view SEM images with EBSD overlay of GaN on a U-grooves with (a) *ff* = 40%, (b) *ff* = 65%, and (c) *ff* = 95%. Each pixel has resolution of 20 × 20 nm, and red, blue, gray colors correspond to h-GaN, c-GaN, and indistinguishable phases, respectively. The crystal orientation of c-GaN is identified and labeled in (c). The white scale bars in the bottom right of each figure correspond to 200 nm. Reprinted from R. Liu and C. Bayram, Appl. Phys. Lett. 109, 38 (2016). with the permission of AIP Publishing.

Figure 24 shows the plane-view EBSD images overlaid on top of SEM images of the (a) $ff = 40\%$, (b) $ff = 65\%$, and (c) $ff = 95\%$ U-grooves. The red, blue, and gray pixels indicate hexagonal, cubic, and indistinguishable crystal phase, respectively, and have the spatial dimension of 20 nm by 20 nm. EBSD identifies and confirms the GaN formed in the middle as the cubic phase, with its (001) plane on the top surface and its (110) , $(1\bar{1}0)$ planes parallel and perpendicular to the U-grooves, respectively. As the *ff* of the U-groove approaches 100%, the surface coverage of c-GaN increases, until the entire surface is composed of only c-GaN, as shown in Figure 24 (c). Electron backscatter diffraction shows that the c-GaN

formed through phase transition in a U-groove is of single phase and proves U-groove nano-patterning is a feasible and reliable method of forming single phase c-GaN surface.

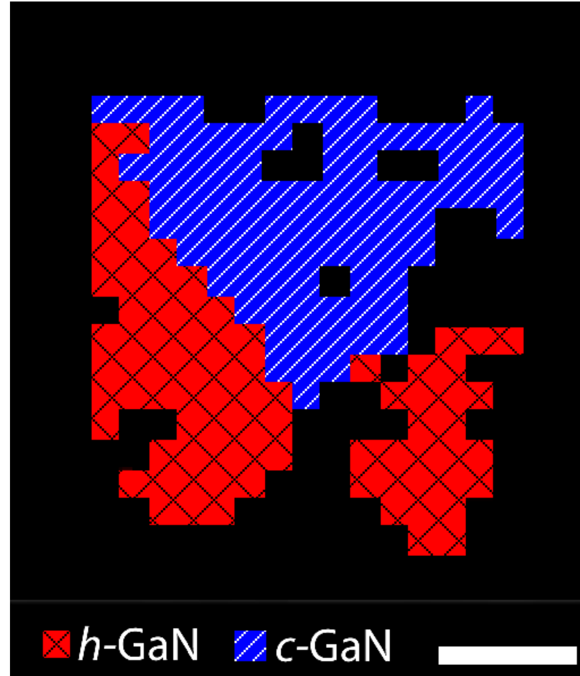

Figure 25 Cross-sectional EBSD image of the *ff* = 95% period. Reprinted from R. Liu and C. Bayram, J. Appl. Phys. 120, 25106 (2016), with the permission of AIP Publishing.

Figure 25 shows the cross-sectional electron backscatter diffraction (EBSD) phase detection of the *ff* = 95% U-groove, showing the GaN phases in red-crossed (hexagonal) and blue-striped (cubic) pixels. It corroborates our modeling (Figure 20 (a)) and shows very clear phase separation after the h-phase crystals coalesced at the bottom of the striped-blue triangle.[29]

Raman spectroscopy is used to study the crystallinity and strain of GaN materials grown in various-sized U-grooves. Using a Horiba Raman Confocal Imaging Microscope with a depolarized 405 nm laser and an 1800 lines/mm grating, Raman spectra of U-grooves with *ff* values ranging from 0% to 205% are collected and plotted in Figure 26 to demonstrate effect of optimization on the crystal quality.

Four peaks in Figure 26 (a) are identified as: Si substrate (520 cm^{-1}), $E_2^H(TO)$ and $A_1(LO)$ of h-GaN (567 cm^{-1}, 733 cm^{-1}), and E_2^H or $A_1(TO)$ of AlN (618 cm^{-1}). Zoomed-in Raman spectra of the TO-

phonons are shown in Figure 26 (b), in which the 558 cm^{-1} peak, attributed to the $E_1(TO)$ Raman shift of h-GaN, is observed. Another peak at 551 cm^{-1} , attributed to TO-phonons of c-GaN, emerges as the *ff* value increases from 0% to 95%, signifying the increasing presence of c-GaN.[72] The peak at 733 cm^{-1} intensifies (Figure 26 (a)), suggesting an involvement of the LO-phonons of c-GaN in addition to the $E_1(LO)$ phonons of h-GaN. Both peaks of c-GaN show a red-shift in their Stokes shift compared to literature (555 and 742 cm^{-1} for TO- and LO-phonons, respectively), indicating c-GaN is under a tensile strain,[72] which is in agreement with other studies.[66,73] At the extreme case of over-deposition (*ff* = 205%), all GaN related Raman signals decrease in intensity and increase in their FWHM, and the TO-phonon Raman mode of c-GaN becomes undetectable. We attribute this to the mixed-phase material on the surface in over-growth samples.[74]

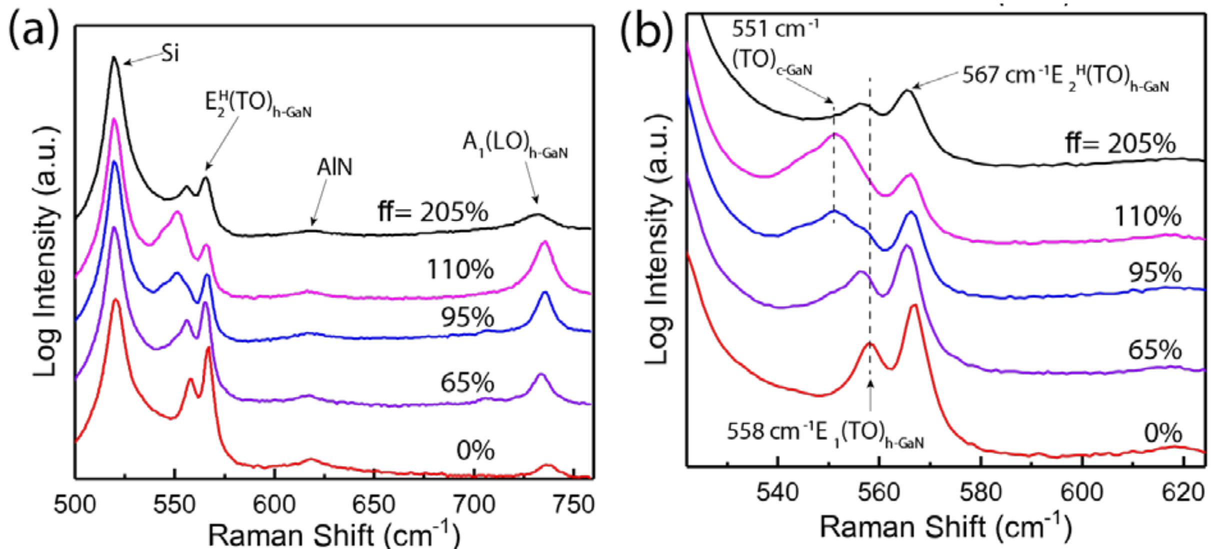

Figure 26 Confocal Raman spectroscopy of U-grooves with *ff* values ranging from 0% (purely h-GaN) to 210% (overgrown-mixed phase GaN). In (a), four peaks are labeled: A_1(LO) and $E_2^H(TO)$ of h-GaN, Si, and A_1(LO) of the AlN nucleation layer. In (b), as phase transition occurs, c-GaN's TO-phonons can be observed. At *ff* = 205%, the extremely over-deposited case, TO-phonon of c-GaN disappears, and the FWHM of h-GaN signal increases, indicating a reduction in crystallinity.[71]

CHAPTER 4

OPTICAL PROPERTIES OF THE PHASE TRANSITION c-GaN

The optical properties of the c-GaN are very important for photonic devices; they indicate the possible quantum efficiency the device can attain and the design parameters that must be taken into consideration prior to device fabrication. In light of this, meticulous optical characterizations are carried out. In the first section, time integrated room temperature PL studies are done to observe the luminescence characteristics of the phase transition c-GaN. The second section is on the study of the Varshni coefficient and the defect centers of c-GaN. The third section calculates the internal quantum efficiency of c-GaN. The forth section focuses on the time-resolved PL study of the c-GaN.

4.1 Room Temperature Light Emission Properties

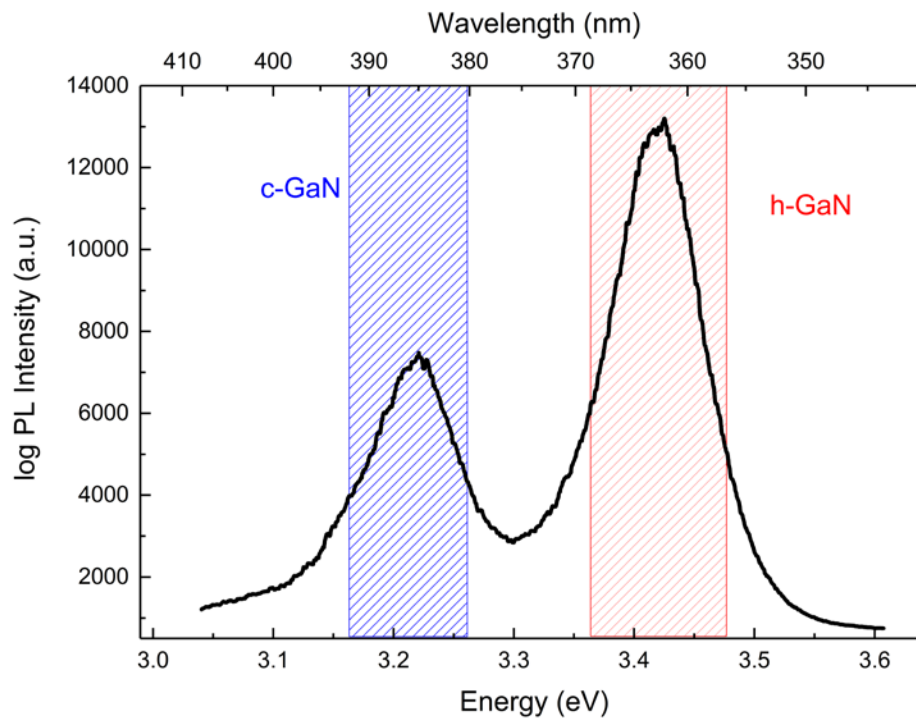

Figure 27 Room temperature PL spectra of the U-grooves. Near band edge emissions of h-GaN at 3.42 eV (362 nm, red) and c-GaN at 3.22 eV (385 nm, blue) are observed. [71]

Time-integrated photoluminescence (PL) is conducted with a frequency tripled Ti:sapphire laser emitting at 266 nm. The signal is collected by a charge-coupled device (CCD) behind a Princeton Instrument spectrometer with a grating with line density of 1200 l/mm and a slit opening width of 1 mm. The data acquisition exposure time is set to 10 seconds. The PL data is shown in Figure 27. Since the laser penetrates through the entire structure, carriers are generated in both c-GaN and h-GaN. The result is the superposition of the spectrum from both phases of GaN. The c-GaN and h-GaN band-to-band luminescence is shown in blue and red striped regions centered at 3.22 and 3.42 eV, respectively.

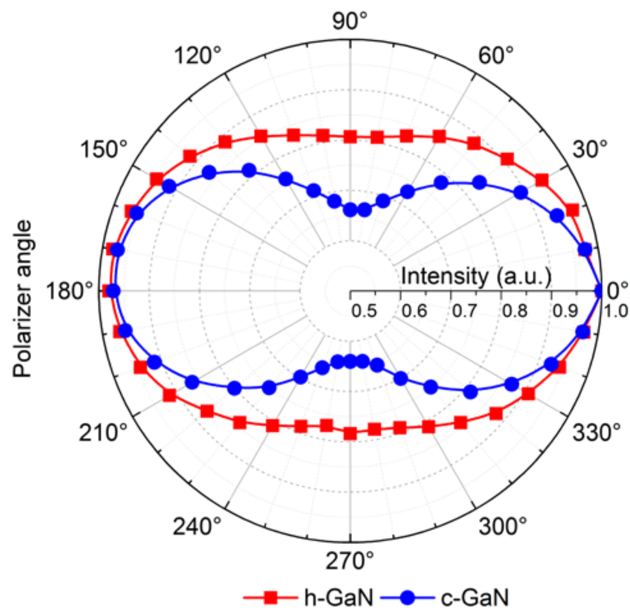

Figure 28 Polarization-dependent photoluminescence of the near band edge emission of h-GaN (red squares) and c-GaN (blue circles). The passing axis of the polarizer angle is parallel to the direction of the U-grooves. The minimum occurs when the polaroid is 90° to the direction of grooves for both materials with c-GaN showing a higher degree of polarization than h-GaN. [71]

Polarization-dependent PL can reveal the nature of the radiative recombination and the escape path of the photons from the material. The phase transition c-GaN in the U-grooves exhibit polarization in the light emitted through either grating-like effect,[75] and/or strain-induced valence band splitting.[76] In this work, the U-grooves are orientated parallel to the passing axis of the polarizer at 0°, and the normalized result is plotted in Figure 28. The wire grid polarizer on glass substrate is placed in front of the spilt opening of the spectrometer to allow light polarized perpendicular to the wire grid through while reflecting others with an

extinction ratio of >100:1 in the near UV range. The band edge emissions from h-GaN and c-GaN are shown by red squares and blue circles, respectively. The emissions from both phases of GaN are linearly polarized in the same direction, which is along the $<11\bar{2}0>$ and <110> directions of h-GaN and c-GaN/Si, respectively. The magnitude of the polarization of the emitted photons is characterized by degree of polarization (ρ), which is:

$$\rho = \frac{I_{\parallel} - I_{\perp}}{I_{\parallel} + I_{\perp}} \tag{3.1}$$

where $I_{\parallel}$ and $I_{\perp}$ are the intensity when the passing axis of the polarizer is parallel and perpendicular to the U-grooves, respectively. The values are found to be 0.12 for h-GaN and 0.20 for c-GaN. The polarization of h-GaN emission (3.42 eV) in a grating-like setting has been reported to have a strong linear polarization parallel to the direction of the grating,[77] which is in good agreement with the results shown in Figure 28. The polarization observed in this work is believed to be the result of a combination of the grating effect and tensile strain, which is determined through Raman studies.

4.2 Varshni Coefficient and Defect Luminescence

Cathodoluminescence is a powerful technique used to study the luminescence properties (spectral accuracy of a few nm) and band structure of materials. Its high spatial resolution (~100 nm) and depth control is suitable for studying the c-GaN on nano-grooved Si. We used a JEOL 7000F analytical Schottky field emission SEM fitted with Gatan MonoCL3 for CL spectroscopy fitted with a spectrometer with 1200 l/mm grating (blazed at 500 nm) and a 1.85 mm slit width (yielding a spectral resolution of ±2.5 nm), and a liquid He stage for temperature control from room temperature to 5.7 K. An electron acceleration voltage of 2 kV is used throughout this study for a maximum electron penetration depth of 42 nm in GaN, according to Kanaya-Okayama[78] formula, to minimize the creation of electron-hole pairs (EHPs) in the underlying h-GaN.

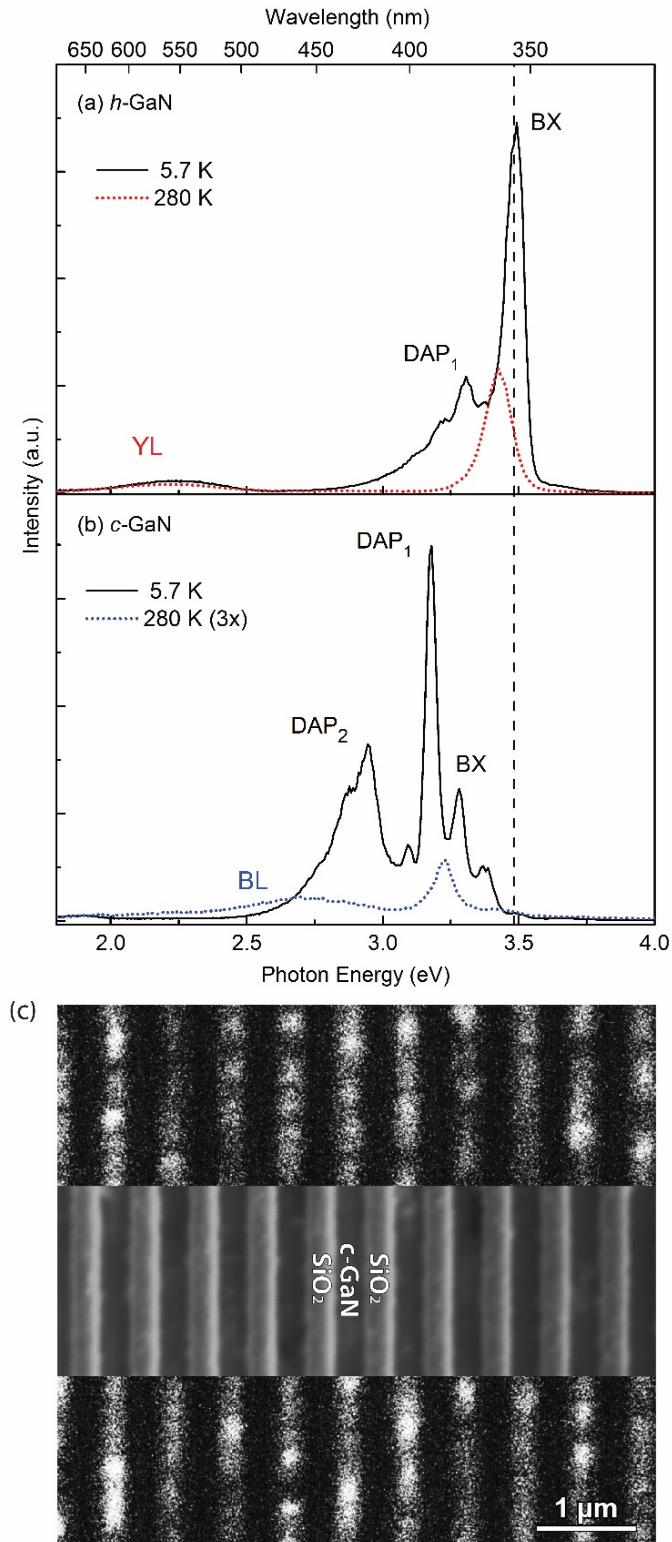

Figure 29 Cathodoluminescence (CL) spectra at 280 K (dotted line) and 5.7 K (solid line) of (a) h-GaN and (b) c-GaN. The dashed line corresponds to the bound exciton (BX) emission of h-GaN at 5.7 K for comparison with c-GaN spectrum. Donor-acceptor pairs ($DAP_{1,2}$) are also present with their LO-phonon replicas observable at 5.7 K. Defect peaks (YL and BL) are also reported. (c) CL overlaid on SEM image of the U-groove shown in (b). Reprinted from R. Liu and C. Bayram, J. Appl. Phys. 120, 25106 (2016), with the permission of AIP Publishing.

Figure 29 shows (a) the CL emission spectrum of SAG h-GaN and (b) the phase transitioned c-GaN at 280 K and 5.7 K taken under 2 nA of electron beam current. The vertical dashed line corresponding to the near band edge (NBE) emissions of h-GaN (BX) at 5.7 K is drawn across the two figures for reference. At 280 K, h-GaN shows a near band edge (NBE) transition at 3.43 eV, and the yellow luminescence (YL) at 2.21 eV. On the other hand, c-GaN shows a NBE transition at 3.22 eV, and another broader transition at 2.72 eV (blue luminescence (BL)). Comparing the h-GaN and c-GaN CL spectra at room temperature, no h-GaN related emission is detected in the c-GaN emission. At 5.7 K, h-GaN shows a bound exciton (BX) transition at 3.49 eV (labeled as BX) and another transition at 3.31 eV (labeled as DAP_1), which other studies attribute to a donor-acceptor pair (DAP) transition.[79] The energy difference between BX and DAP_1 implies an acceptor level of ~180 meV (using $E_D \approx 25$ meV, $E_{exciton} \approx 26$ meV). LO-phonon replicas are observable at ~90 meV intervals lower than the zero-phonon emission.[80] Similarly, c-GaN Figure 29 (b) shows a BX emission at 3.28 eV, and three other emission peaks at 3.18 (DAP_1), 3.08, and 2.95 eV (DAP_2). DAP_1 transition has been identified as (D^0, A^0) transition in literature.[81] The energy difference between BX and DAP_1 yields an acceptor energy of ~100 meV, which is in line with literature.[82] DAP_2 emission is observed at a lower energy (~ 230 meV) than DAP_1, suggesting another deep level transition.

In order to understand and study these luminescence centers, temperature-dependent cathodoluminescence (TDCL) is conducted. Figure 30 shows (a) the TDCL spectra of h-GaN and (b) c-GaN carried out from 280 K to 5.7 K. The dashed lines represent the peak position of BX at 5.7 K for reference.

As temperature decreases to below 140 K, DAP_1 peak of h-GaN becomes distinguishable along with very strong LO-phonon coupling (Figure 30 (a)). This transition is believed to be associated with a shallow acceptor of either Si_N or C_N.[83] At roughly the same temperature, DAP_1 and DAP_2 of c-GaN also become visible (Figure 30 (b)), but DAP_2 shows a much stronger LO-phonon coupling than DAP_1. The DAP_1 of c-GaN exhibits an increase in energy with increasing temperature. Literature suggests this is due to the

thermal ionization of the donors at higher temperature that turns the donor-acceptor transition (D^0, A^0) into a free to acceptor transition (e, A^0).[84]

At T< 60 K, the unlabeled peak at ~3.08 eV with a much weaker intensity is resolved. This peak has been attributed to free-to-bound (e, A^0) or another donor-acceptor pair (D^0, A^0) related to carbon residuals or arsenic.[85] As most studies on c-GaN luminescence are performed on GaAs substrates, and their respective emissions at this energy level are very strong. The relatively weak emission at this wavelength on our c-GaN on Si(100) supports the postulation of As as an additional acceptor level. The origin of the DAP_2 peak in c-GaN is more controversial. Earlier work[86] have attributed this peak to a LO-phonon replica of the 3.08 eV peak on c-GaN/GaAs, but our c-GaN/Si sample shows this is not the case. Particularly, the intensity of the zero-phonon line of DAP_2 is many factors greater than the 3.08 eV emission.

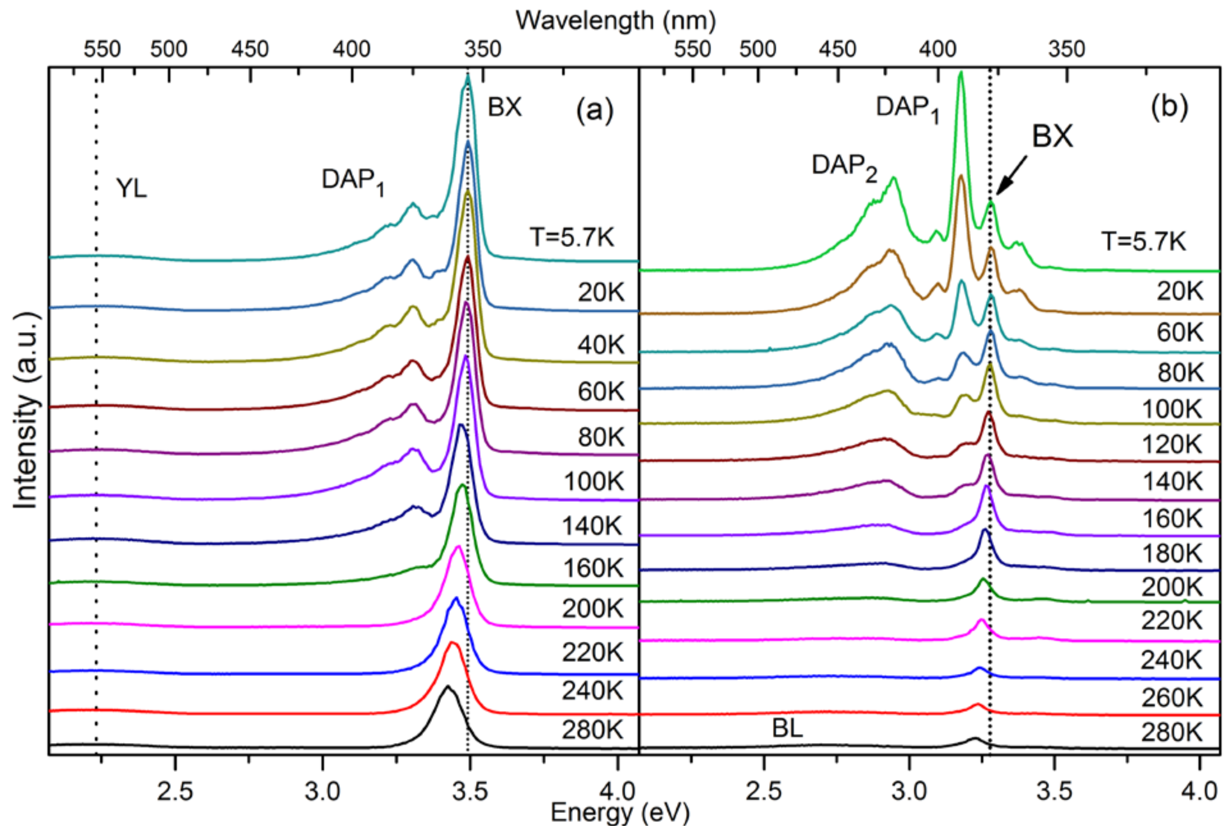

Figure 30 Temperature dependent CL spectra of (a) c-GaN and (b) h-GaN from 280 K to 5.7 K. At 280 K, near band edge emission (BX) of c- (h-) GaN is observed at 3.22 (3.43) eV, whereas at 5.7 K it blueshifts to 3.28 (3.49) eV. At temperatures below 140 K, donor-to-acceptor emission peaks (DAP_1 and DAP_2) appear, and below 60 K, LO-phonon replica emissions become pronounced. The dashed lines are the peak position of BX at 5.7 K drawn across figures for guidance. Reprinted from R. Liu and C. Bayram, J. Appl. Phys. 120, 25106 (2016), with the permission of AIP Publishing.

Throughout our measurements, the YL luminescence line, which is commonly believed to be associated with native defects such as V_{Ga} and its complexes ($V_{Ga}O_N$, $V_{Ga}C_N$, $V_{Ga}Si_{Ga}$),[87] remained relatively stable in intensity and emission energy as the temperature is reduced. This behavior is similar to those reported in literature.[88] The BL of c-GaN becomes embedded in DAP_2 and its LO-phonon replicas at lower temperature, and could not be uniquely resolved.

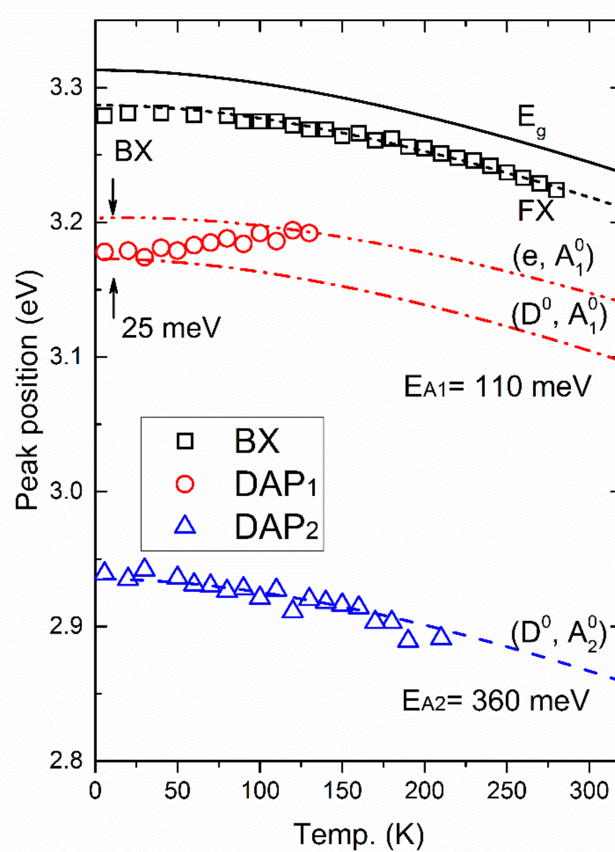

Figure 31 Temperature-dependent CL peak positions of free exciton (FX) transitions (squares) and DAP_1 (circles) and DAP_2 (triangle) of c-GaN. The bandgap energy (E_g, solid black line) is calculated and fitted by Varshni's equation ($\alpha = 6.83 \times 10^{-4}$ eV/K and $E_0 = 3.31$ eV). At the lowest temperatures, FX transitions shifts to a bound exciton (BX) transition with a binding energy of a few eV. DAP_1 transitions from a donor-acceptor pair (D^0, A_1^0), with an acceptor energy of 110 meV and a donor energy of ~25 meV, to a free-to-acceptor (e, A_1^0) transition as the temperature increases. DAP_2 shows a donor-acceptor pair (D^0, A_2^0) transition with acceptor energy of E_{A2} = 360 meV. Reprinted from R. Liu and C. Bayram, J. Appl. Phys. 120, 25106 (2016), with the permission of AIP Publishing.

To find the temperature dependence of the three peaks (BX, DAP_1, DAP_2) of c-GaN, their energies are plotted against temperature in Figure 31. The exciton emission (BX) can be used in conjunction with the excitonic binding energy ($E_{exciton}$) to calculate the bandgap at a specific temperature. The temperature dependence of the bandgap of h-GaN and c-GaN is modeled with Varshni's equation:[89]

$$E(T) = E_0 - \frac{\alpha T^2}{(T+\beta)} \tag{3.2}$$

where E_0 is the bandgap at zero temperature, α is the Varshni's coefficient, and β is taken as the Debye temperature of GaN (600 K). The least square fit yields $E_0 = 3.31\,(\pm\ 0.01)$ eV and $\alpha = (6.83 \pm 0.22)\times 10^{-4}$ eVK^{-1} for c-GaN ($E_0 = 3.51\ (\pm 0.01)$ eV and $\alpha = (7.37 \pm 0.13)\times 10^{-4}$ eVK^{-1} for h-GaN), similar to the work done on other substrates.[90–92] The small deviation at the lowest temperatures is caused by the free excitons binding to a lattice site to become bound excitons (BX). DAP_1 peaks are fitted with two different types of transitions: (e, A^0), shown as red dot-dot-dash line, and (D^0, A^0), red dot-dash line. Their energies are calculated using:

$$h\nu\left(e, A^0\right) = E_g(T) - E_D + \frac{1}{2}kT \tag{3.3}$$

for free-to-acceptor transitions, and

$$h\nu\left(D^0, A^0\right) = E_g - E_D - E_A + \alpha N^{\frac{1}{3}} \tag{3.4}$$

for donor-acceptor transitions, where

$$\alpha = \left(\frac{4\pi}{3}\right)^{\frac{1}{3}} \times \frac{e^2}{4\pi\varepsilon\varepsilon_0} \tag{3.5}$$

N is the dopant concentration, α is a material property (for GaN ($\varepsilon = 9.7$), $\alpha = 2.39\times 10^{-8}$ eV cm). Using a typical impurity concentration of 10^{16} cm^{-3} for unintentionally doped GaN, the last term in Equation (3.4) is about 5.1 meV. Least square fitting with these parameters reveals an acceptor level of $E_{A1} \approx 110$ meV for DAP_1, and $E_{A2} \approx 360$ meV for DAP_2 (blue dashed line). We attribute DAP_2 to intrinsic defects such as gallium vacancy (V_{Ga}), as it is a common defect in MOCVD-grown material suggested by the literature.

As shown by Raman spectroscopy and EBSD, the *ff* = 95% is the most optimized U-groove sample for c-GaN, and provides the largest surface coverage of phase-transition c-GaN with the highest crystal quality. As such, CL study conducted on this U-groove configuration reveals the optical properties of the highest quality c-GaN enabled via phase-transition. Figure 32 shows the CL spectrum of the *ff* = 95% U-

grooves conducted at 5.7 K with variable electron beam current in raster scan mode, which gives a good representation of the luminescence properties of the top 47 nm layer over a 20×30 μm^2 area.

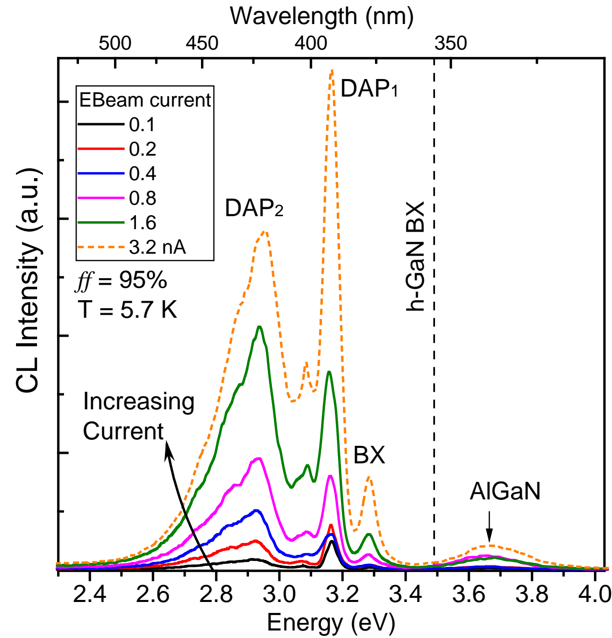

Figure 32 Low temperature CL spectra of the c-GaN. Bound exciton (BX) at 3.28 eV, two donor-acceptor pairs at 3.18 (DAP_1) and 2.95 (DAP_2) eV, as well as their LO-phonon replicas, of c-GaN are observed. A band-to-band like emission at 3.67 eV with FWHM = 220 meV is also observed. No h-GaN emission at 3.48 eV (vertical dashed line) is detected, indicating no h-GaN incursions.[71]

Three luminescence centers are observed and identified as: bound exciton (BX), donor acceptor pairs (DAP_1 and DAP_2) at 3.28, 3.17 and 2.95 eV, respectively. LO-phonons of the DAPs are also observed at energy intervals of ~ 90 meV from the zero-phonon line, with DAP_2 showing a stronger phonon-coupling due to the deeper acceptors involved, as expected. No luminescence at 3.48 eV, which is the excitonic recombination of h-GaN, is observed. A broad emission centered at 3.67 eV with a FWHM of 220 meV is reported. Injection current dependent CL is used to determine the nature of this radiative recombination center. Power-law study reveals a linear relationship between its intensity $(I_{CL}^{3.6eV})$ and injection current (J_b) with a slope of 0.9 ± 0.2, which indicates an unsaturated, band-to-band like transition across the injection current range of 0.1 to 3.2 nA $(I_{CL}^{3.67eV} \propto J_b^{0.9})$.[93] Since the emission energy is above both cubic and hexagonal phase GaN, it is likely from neither crystal phases. We attribute this to the presence of the

exposed AlN nucleation layer on the SiO_2 sidewalls, considering the persistent AlN phonon shifts observed in Raman spectroscopy (Figure 26) across different *ff* values.

Cathodoluminescence imaging was conducted to investigate the spatial distribution of the luminescence centers at 5.7 K. High-magnification SEM images of grooves with various *ff* values ranging from 30% to 205% are shown in Figure 33a and a large-scale SEM image is shown in Figure 33 (b). The monochromatic CL images of the grooves shown in Figure 33b at: λ = 355 nm (3.49 eV, h-GaN BX), 390 nm (3.18 eV, c-GaN DAP_1) and 420 nm (2.95 eV, c-GaN DAP_2), are shown in Figure 33(c), 33(d), 33(e), respectively.

The luminescence of h-GaN BX (Figure 33c) in the undergrown U-grooves (*ff* = 30% and 40%) show very uniform and intense luminescence, which indicates the presence of h-GaN on the surface, while the intermediate U-grooves (*ff* = 65%, 70%, 90%) show a decreasing amount of luminescence at this energy, indicating the decreasing amount of h-GaN that is excited within the top ~ 47 nm layer.

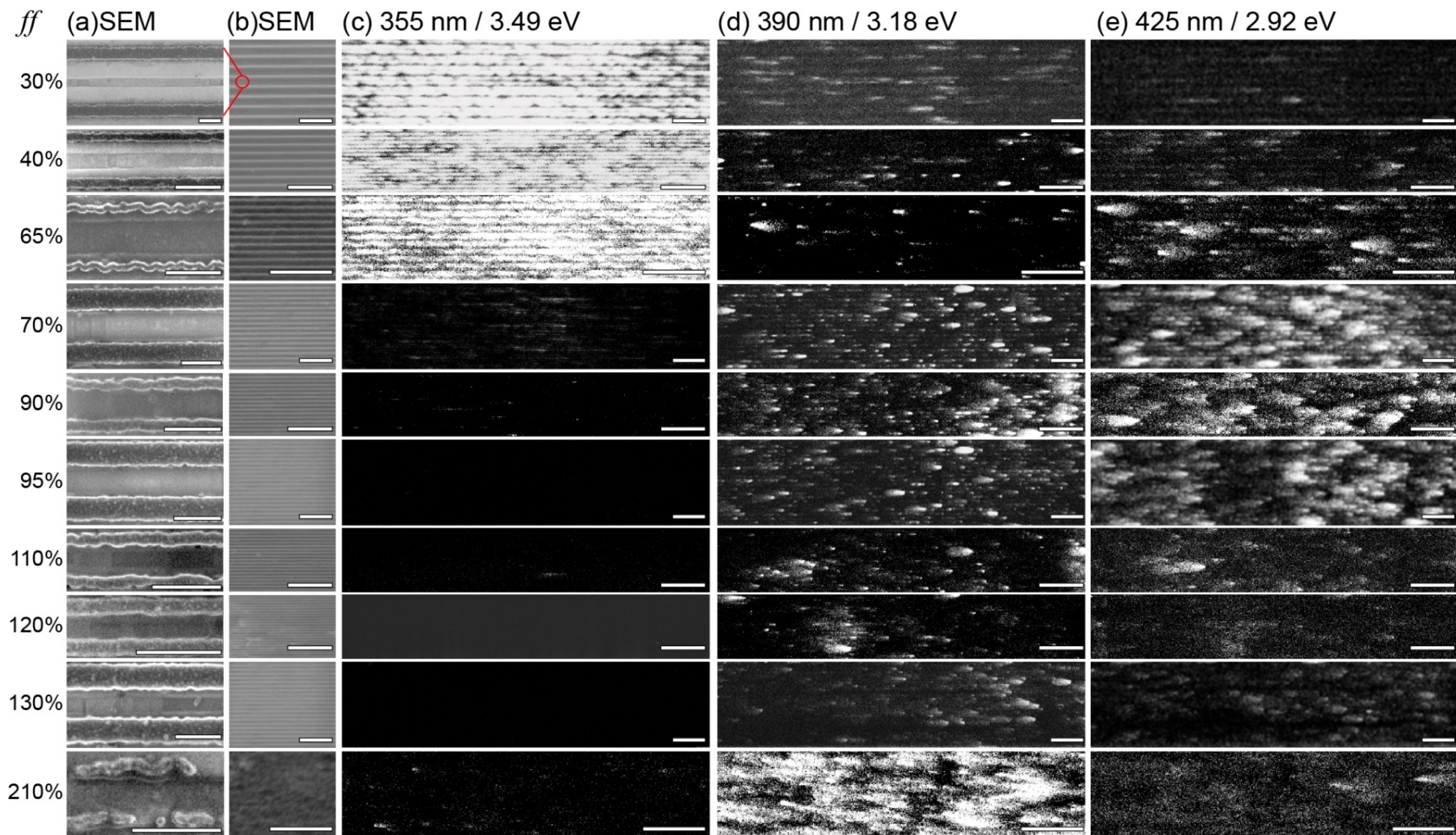

Figure 33 Plain view SEM and CL images of GaN on various U-grooves. (a) High magnification SEM images with scale bar of 500 nm. (b) Low magnification SEM image, and its corresponding monochromatic CL images at (c) the bandgap of h-GaN at 355 nm, (d) DAP_1 of c-GaN at 390 nm, and (e) DAP_2 of c-GaN at 425 nm.[71]

The most optimized U-grooves, *ff* = 95%, show no observable h-GaN emission, indicating a very good coverage of the c-GaN triangle on the surface. Beyond the optimized condition for phase transition at *ff* = 100%, traces of h-GaN BX luminescence can be observed scattered randomly across the image, indicating a reappearance of h-GaN in an irregular distribution. The luminescence of DAP_1 (Figure 33 (d)) of c-GaN at 3.18 eV can be seen scattered randomly across the images in small and bright clusters. The intensity and concentration of these clusters seem to have a weak dependence with *ff*. At the extreme end of overgrowth (*ff* = 205%), the concentration of DAP_1 increases dramatically, but the cluster-like distribution persists. This suggests an increase in point defect formation (e.g. lattice site vacancies, V_{Ga}, V_N) or slip planes (e.g. basal stacking faults) rather than extrinsic impurity (C, O, etc.) since the growth condition has not changed between the U-grooves. The formation of stacking faults is directly observed in Figure 23 (b) near the c-GaN/oxide interface. The luminescence of c-DAP_2 (Figure 33 (e)), while showing a similar cluster-like distribution observed in c-DAP_1, follows the trend of the cubic optimization. It is at its strongest when *ff* is the closest to 100%, and becomes weaker as *ff* deviates from 100%. This suggests this luminescence center is unique to crystalline c-GaN, and is not observed when a large degree of phase mixing or poor crystalline quality is present.

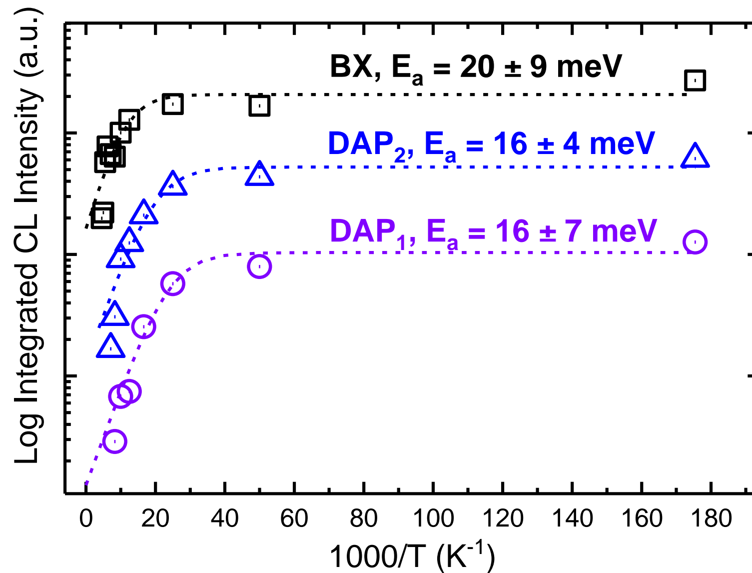

Figure 34 Arrhenius plot of c-GaN CL emissions at 5.7 K. Fitting shows activation energy of 20 ± 9, 16 ± 7, 16 ± 4 meV for BX (exciton binding energy), DAP1 (shallow donor), DAP2 (shallow donor) respectively.[71]

Temperature-dependent CL can be used to calculate the energies of the donors and acceptors involved in DAP_1 and DAP_2. Figure 34 shows the Arrhenius plot of the integrated CL intensity of the three luminescence centers of c-GaN. The integrated intensity obeys:[94]

$$I(T) = \frac{I_o}{1 + C \exp(-E_{act} / k_B T)} \tag{3.6}$$

where I_0, C are fitting constants, k_B is the Boltzmann's constant, and T is the temperature. Fitting of the experimental data reveals donor activation energy (E_{act}) of 20, 16, and 16 meV for BX (black squares), DAP_1 (violet circles), and DAP_2 (blue triangles), respectively. The activation energy for bound exciton corresponds to the excitonic binding energy of ~ 20 meV. The similarity between the activation energies obtained for the DAPs implies these transitions involve the same shallow donor, which is believed to be silicon. Using the estimation of the shallow donor activation energy, bandgap of c-GaN at 0 K[29], and the energies of photon emitted, the calculated acceptor energies are 124 meV (DAP_1) and 344 meV (DAP_2). The shallow acceptor at 146 meV above the valence band is of particular interest, as it demonstrates the possibility of a much higher p-type doping efficiency and conductivity of c-GaN than that of h-GaN. A proposed band diagram of c-GaN is shown in the inset in Figure 35.

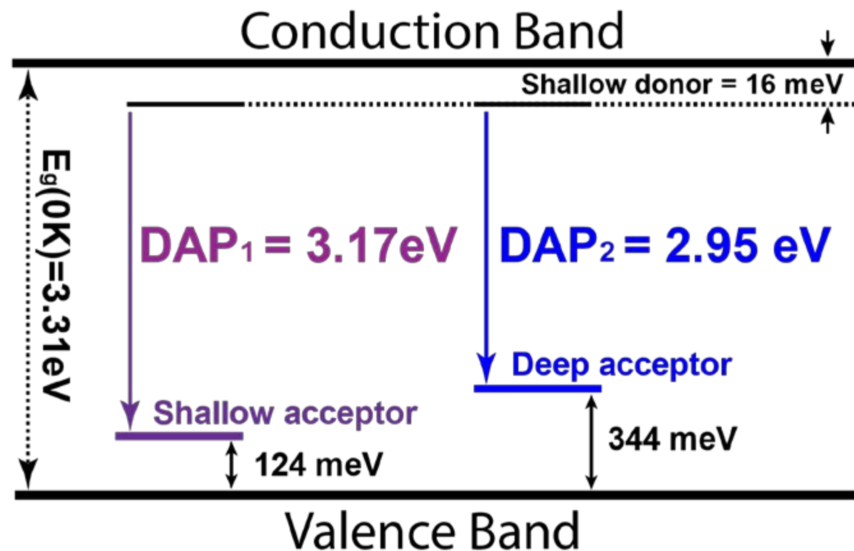

Figure 35 Proposed band diagram for the phase transition c-GaN.[71]

4.3 Quantum Efficiencies

The internal quantum efficiency (IQE) provides insight to how efficient the radiative recombination process is compared to other non-radiative recombination mechanisms (e.g. Shockley-Reed-Hall, Auger), and how well these undesired carrier loss paths are suppressed in a photonic device. Using the results from the CL study, IQE of the band-to-band transition of h-GaN (3.48 eV) and c-GaN (3.28 eV) is calculated using:

$$\eta_{IQE}(T) = \frac{I(T)}{I(5.7\text{K})} \quad (3.7)$$

where $I(T)$ is the integrated intensity as a function of temperature and $\eta_{IQE}(T)$ is the internal quantum efficiency, assuming the non-radiative recombination centers are fully deactivated at 5.7 K.[95] The estimated IQE for the optimized phase transition c-GaN band-to-band transition is plotted as a function of temperature in Figure 36 (right), which shows a highest obtained IQE of 29% at room temperature.

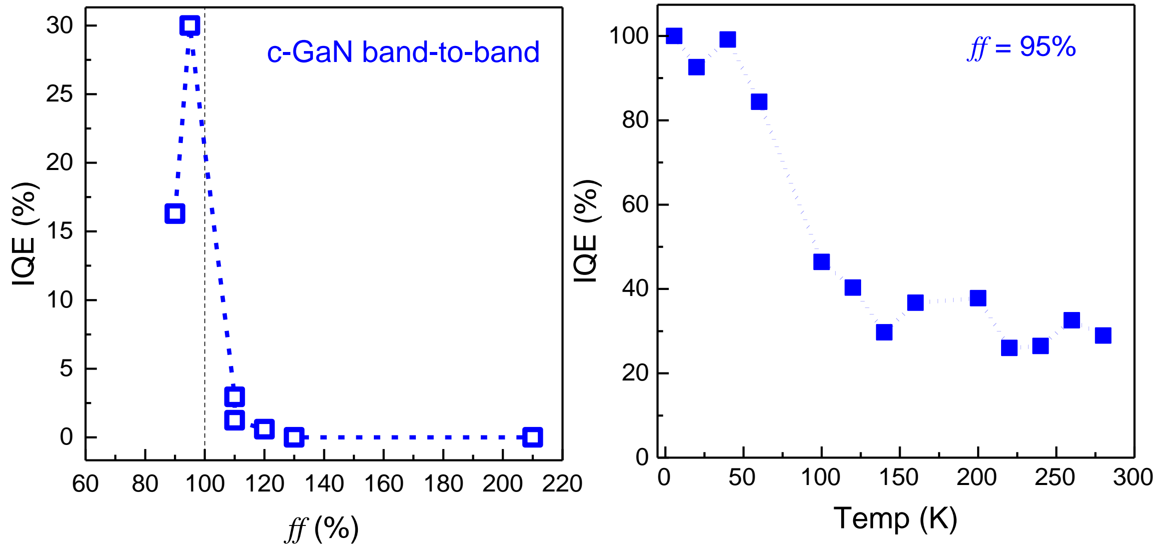

Figure 36 Internal quantum efficiency of the c-GaN band-to-band emission. (Left) Effect of optimization on the c-GaN IQE. The dashed line represents the theoretical fully optimized U-groove, which coincides with the highest IQE obtained. (Right) the temperature dependence of the IQE of the of the *ff* = 95% U-grooves.[71]

The Figure 36 (left) shows the IQE of c-GaN for various *ff* from 0% (pure h-GaN) to 210% (the U-grooves shown in the bottom row of Figure 33). The IQE for c-GaN increases very rapidly as the value of *ff* approaches 100%, and drops down to very small values once the value of *ff* exceeds unity. The IQE and

CL imaging suggest the importance of U-pattern optimization and regrowth height. If GaN is under-deposited, c-GaN is unable to cover the entire surface, resulting in poor quantum efficiency. If GaN is over-deposited, defect formation dominates the material growth, resulting in poor quantum efficiency. There exists a relatively small window in which IQE is maximized for c-GaN crystals given a specific U-groove. This is when complete c-GaN coverage is achieved through the condition described in Equation (2.17).

4.4 Radiative Lifetime

We perform time-resolved photoluminescence (PL) studies to investigate the luminescence lifetimes in h- and c-GaN. The luminescence lifetime can reveal the carrier loss mechanisms and quantitatively compare their rate, and how suitable the material is for photonic applications. The measured PL lifetime (τ_{PL}) is related to the radiative lifetime (τ_{rad}) and nonradiative lifetimes (τ_{nr}) through:

$$\tau_{PL}^{-1} = \tau_{nr}^{-1} + \tau_{rad}^{-1} \tag{3.8}$$

It is known that the radiative lifetime in semiconductors is determined by the scattering from the excitonic branch to the photonic branch of the exciton-polariton dispersion curves. Hence, the radiative lifetime for a 200 nm thick GaN film can be expressed as:[96]

$$\tau_{rad} = \frac{1}{2}\left(\frac{5\pi}{3}\right)^{3/5}\left(\frac{M}{\nu_0}\right)^{2/5}\left\{\frac{\hbar^2 c^7 \alpha_p L^3}{C^4 \omega^6}\right\}^{1/5} \tag{3.9}$$

where M / ν_0 is the mass per unit volume of the unit cell (3 kgm^{-3}), α_p is the polarizability (4×10^{-5}), L is the thickness of the excited layer (~ 200 nm), $\hbar\omega$ is the photon energy of the excitonic transition (3.42 eV), and C is the deformation potential (4 eV).[97] This equation yields a theoretical radiative lifetime of ~ 470 ps for h-GaN. The corresponding radiative lifetime of c-GaN is estimated to be ~47 ps – an order of magnitude shorter than that of h-GaN, in line with other works.[98,99] We believe this is because of a greater electron-hole wavefunction overlap, which results in a greater oscillator strength, in the absence of polarization fields in c-GaN.

With respect to (non)radiative lifetimes, the literature has shown through temperature-dependent PL measurements that c-GaN has radiative and non-radiative lifetimes that are about an order of magnitude shorter than those of h-GaN.[98] Various works claim that the internal electric field in h-GaN strongly decreases the oscillator strength via quantum confined stark effect.[99,100] PL studies on the quantum dots (QDs) revealed that the internal polarization fields are responsible for the difference in PL lifetimes between h-GaN and c-GaN. The diameter of c-GaN QDs was reported to have very little effect on its radiative lifetime, due to the wavefunction overlap being largely unchanged. This is in contrast to the drastic reduction in radiative efficiency (from 80% to 25%) observed in h-GaN QDs with increasing diameters (from 25 Å to 36 Å). This is a direct observation of the detrimental consequence of electron and hole wavefunction separation caused by the internal electric field in h-GaN. As such, the authors found a radiative lifetime that is one order shorter in c-GaN than that of h-GaN.

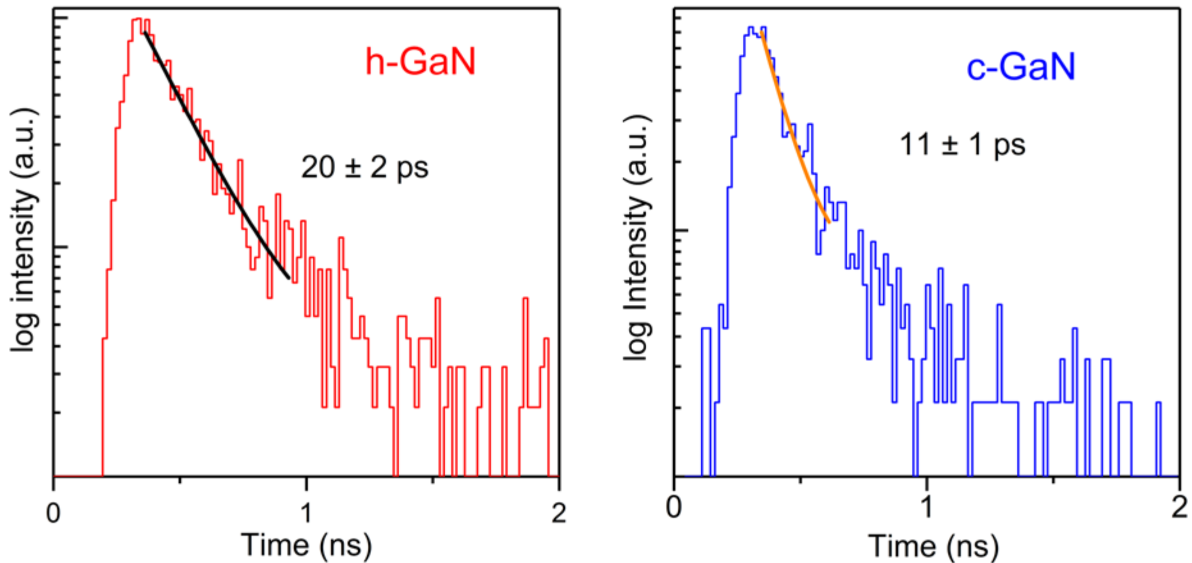

Figure 37 Time-resolve photoluminescence of the bandgap emission of (left) h-GaN and (right) c-GaN. [71]

Experimentally, time-resolved PL (TRPL) study is carried out at the Center for Nanoscale Materials Argonne National Laboratory with a frequency tripled Ti:sapphire laser (λ = 266 nm, 80 MHz, 150 fs pulse width) and a Hamamatsu universal streak camera system with temporal resolution of <1 ps to investigate the carrier dynamics of phase-transition c-GaN. Figure 37 shows the TRPL data for h-GaN (left) and c-

GaN (right), which correspond to the free exciton transitions of h-GaN (3.42 eV) and c-GaN (3.22 eV), respectively.[29] Time resolved PL intensity shows an exponential decay with lifetimes of 20 ps for h-GaN and 11 ps for c-GaN.

Studies have shown that lateral epitaxial overgrowth h-GaN on sapphire exhibits a radiative lifetime in the range of 80 ~ 210 ps at room temperature,[101,102] and 530 ps for GaN grown by hydride phase vapor epitaxy (HVPE).[103] For c-GaN, studies reported extremely short PL lifetime of ≈ 15 ps.[104] For h-GaN, our data shows an extremely fast decay compare to the high-quality material in the literature, suggesting an additional carrier loss mechanism in the U-grooves. However, the phase-transition c-GaN shows a comparable PL decay lifetime to the 1 μm thick c-GaN films on 3C-SiC, indicating a similar carrier recombination rate.[104]

Using Equation (3.8) and theoretical τ_{rad} of 470 μs (47 μs) for h-GaN (c-GaN), the nonradiative decay dominates the transition with τ_{nr} of 21 ps (14 ps) for the h-GaN (c-GaN) in the U-grooves. We believe that the short PL lifetimes of the two phases of GaN in the U-grooves are dominated by two mechanisms: material interfaces for h-GaN and strong oscillator strength in c-GaN. The stacking faults along the hexagonal-cubic phase transition interfaces may act as nonradiative recombination centers.[105] The h-GaN–silicon and c-GaN–air interfaces may also provide another carrier loss mechanisms. On the other hand, a fast PL lifetime could also be the result of a strong radiative recombination resulting from the higher degree of confinement provided by quasi 1D nature of the U-grooves. It has been reported that c-GaN has a significantly stronger oscillator strength with its smaller bandgap and the lack of polarization fields.[98]

Another approach to estimate τ_{rad} of c-GaN is to utilize the IQE calculated from Section 4.3. Using IQE = 29% and the measured $\tau_{PL} = 11$ ps of c-GaN, the τ_{rad} is extracted using Equation (3.10)

$$\eta_{IQE} = \frac{\tau_{PL}}{\tau_{rad}} \tag{3.10}$$

which yields a τ_{rad} of 38 ps, which is ~12.4 times shorter than the value for h-GaN. The finding in the TRPL for c-GaN is in good agreement with the other studies in the literature.

Fundamental material properties can be extracted using the observed radiative lifetime (38 ps) and Equation (3.9). Assuming similar mass density and deformation potential between h-GaN and c-GaN, the polarizability, α, can be calculated for c-GaN using the 3.22 eV for ω and 200 nm for L. The polarizability of c-GaN is calculated to be 8.3×10^{-11}, which is approximately seven orders of magnitude smaller than that of h-GaN.

CHAPTER 5

PHOTONICS OUTREACH ACTIVITIES

To broaden our community outreach, we are developing a theme-based interactive "solid-state lighting" outreach program, which we will be piloting at a local middle school with a large underrepresented student presence. A portable exhibit will be devised to educate K-12 students, as well as the general public about solid-state lighting. It involves making electrical contact with LED structures on an uncut wafer, then measuring the efficiency using an integrating sphere while comparing it with conventional light sources.

5.1 Intra-Institutional Educational Outreach

We are currently working on the development of a brand-new course on solid-state LEDs and solar cells at the Electrical and Computer Engineering department of University of Illinois at Urbana Champaign. It has been beneficial to work as the cleanroom teaching assistant to demonstrate and supervise the students on the characterization of LED devices and III-nitride materials. The lab modules are split into six modules that take one to three weeks each. These modules include: (i) safety walk-through, (ii) SEM characterization, (iii) LED electrical testing using parametric analyzer and optical testing using optical fiber spectrometer, (iv) temperature-dependent electrical and optical testing of LED with a heating stage, (v) solar cell electrical testing using parametric analyzer and external quantum efficiency test using Oriel's QEPVSI-b quantum efficiency measurement system, and (vi) temperature-dependent electrical testing of solar cells with a heating stage. The course has been upgraded from a temporary, experimental course to a permanent one with the code: ECE443 as of September 2017.

5.2 Inter-Institutional Outreach Activities

The goal to advance NSF's mission to disseminate the knowledge about photonics has involved mentoring the NSF's REU and Research Experience for Teachers (RET) program participants during the summers of 2016 and 2017 at UIUC. The mentorship consists of demonstrating graduate-level photonics research and supervising the participants as they engaged in hands-on research activities (cleanroom wet chemistry, low-temperature Hall effect measurements, and using the scanning electron microscope). The participants learned to perform data analysis in OriginPro and MATLAB. At the end of the program, the REU participants were assisted with poster presentation preparation, and the RET participants in developing a junior/senior high school level physics experiment in solid-state lighting: measuring the width of a piece of hair using a laser pointer, and taking a LED chip apart to find the GaN semiconductor. Based on the very positive feedback received in the summer of 2016, improvements are being made in the lab in order host future summer research programs for a K-12 teacher (RET) and an underrepresented student from the nano@illinois program (REU); our new laser setup will facilitate more hands-on experience and involvement for the visitors.

Collaboration with the physics department from Colorado College on setting up volunteering research for physics undergraduates over the summer via the NSF's REU program. Over the summer we conducted temperature-dependent PL experiments and PL intensity mapping of as-grown InGaN LEDs. In addition to characterization experiments, we conducted fabrication technique development such as: silicon oxide growth optimization and potassium hydroxide anisotropic etching of silicon wafers. We also designed a photolithography mask for future fabrication of c-GaN LED.

CHAPTER 6

CONCLUSION

6.1 Preliminary Research Findings

We demonstrate that phase transition of h-GaN to c-GaN is a reliable c-GaN single-crystal growth technology that can be precisely controlled by substrate patterning and material deposition. High crystallinity and uniformity phase transition c-GaN surface can be reproduced when the critical condition, $h_c = (1.06p - 0.75t_d)/(1 - \tan\alpha / 0.71)$, is met, as shown by the SEM, EBSD, TEM study. Raman spectroscopy of the phase transition c-GaN shows the material is under tensile-strain, and its light emission has a 0.2 degree of polarization along the pattern direction. At 280 K, c-GaN (h-GaN) shows a near band edge luminescence at 3.22 eV (3.43 eV) and a defect peak at 2.72 eV (2.21 eV), and at 5.7 K, bound exciton transition at 3.28 eV (3.48 eV), donor-to-acceptor transition at 3.18 eV (3.31 eV) and another peak identified as (D^0, A^0) transition at 2.95 eV. The bandgap energy for c-GaN (h-GaN) of 3.31 eV (3.51 eV) and the Varshni coefficient $\alpha = (6.83 \pm 0.22) \times 10^{-4}\ eV/K$ $((7.37 \pm 0.13) \times 10^{-4}\ eV/K)$ are calculated.

Two defect luminescence centers at 144 and 344 eV above the valence band are identified, and imaging of the distribution of these acceptors suggests these are intrinsic defect and extrinsic impurity levels, respectively. The band-to-band emission of phase-transition c-GaN internal quantum efficiency is calculated independently via temperature dependent CL and time-resolved photoluminescence to be between 23% - 29%, making this technology suitable for next-generation photonic devices.

6.2 Future Work

The high IQE demonstrated by the c-GaN is a promising result for high-performing photonic devices. The next step to bring this technology to fruition is to fabricate interdigitated light emitting diodes across

multiple periods of U-groove, as shown in Figure 38. LED active layer stack can be grown on the c-GaN template provided by the U-grooves (shown on the left). Standard dry etching techniques can etch away the LED stack to reveal the N-type layer. N- and P-contact (with transparent thin current spreading layer) fingers can then be deposited across multiple U-grooves to create an active volume with arbitrary active volume. An interdigitated design (shown on the right) can allow the fabrication of large area devices with good electrical spreading efficiency.

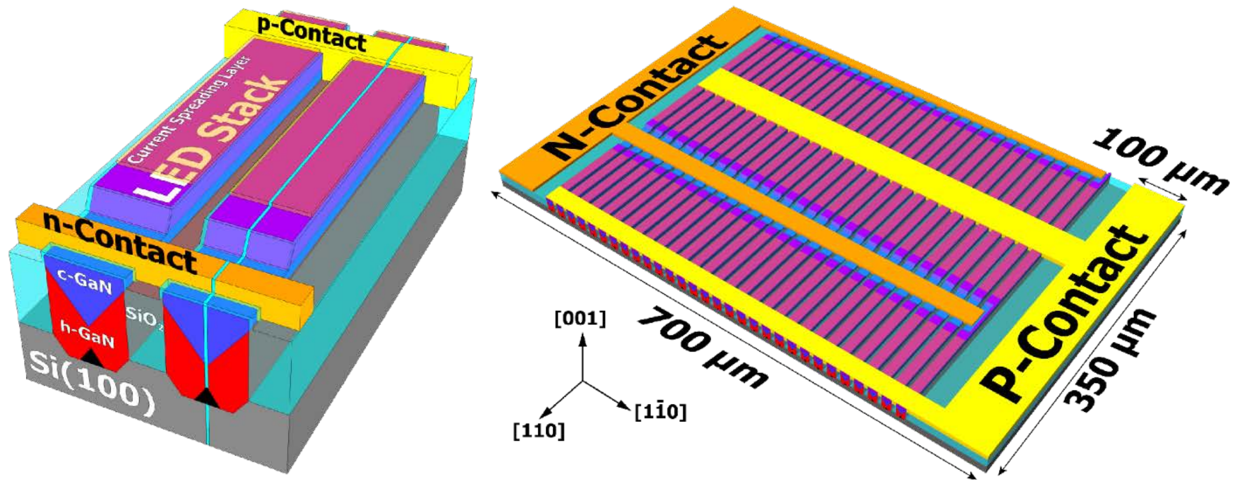

Figure 38 LEDs based on the phase transition c-GaN in U-grooves. (Left) N- and P-contact fingers can span across multiple periods of U-groove to create a larger device. (Right) 3D schematic of an interdigitated LED that is made of many U-grooves.

Other photonic devices, such as a AlGaN-based UV Fabry-Perot edge emitting laser, can also be fabricated in the U-grooves, as shown in Figure 39. A UV laser can be fabricated on the U-groove in similar design as a ridge-wave guide laser. Since the substrate can be conducting silicon, it is possible to use the back side of the substrate as a contact, which devices fabricated on sapphire substrates cannot.

In order to utilize the c-GaN for laser applications, the extension of this master's thesis to a PhD dissertation will encompass (1) photonic device design simulation, (2) quantitative investigation of structure-emission correlation, (3) device fabrication, and finally (4) optoelectronic characterization of photonic devices.

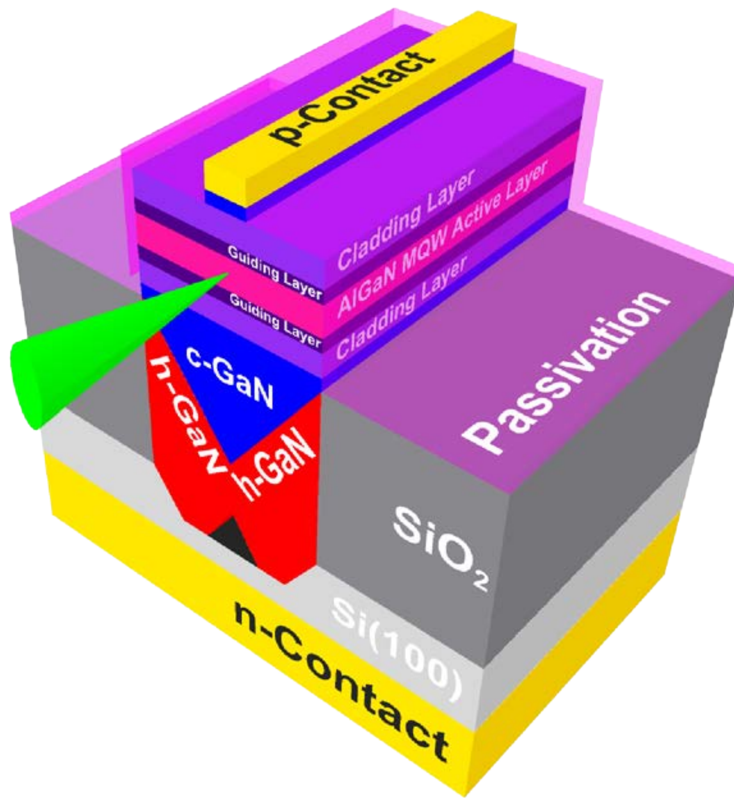

Figure 39 Fabry-Perot edge emitting laser diode fabricated on the phase transition c-GaN in a U-groove.

6.2.1 Laser Design Simulation

The goal is to determine the optimal optical properties and electrical properties of the LD device structure by using technology CAD (Synopsys Sentaurus, RSoft, or Crosslight).

Schrodinger's equation will be solved using the numerical simulation with varying (i) number of quantum wells, (ii) the composition of the wells and barriers, (iii) width of the wells, and (iv) graded confinement. Vegard's law will be used to find the bandgap of the active and barrier region as well as the conduction and valence band offsets at the heterojunctions to find the ground energies of the quantum well. Next is finding the correct amount of compressive strain to limit the optical transition to transverse electric polarization only in order to minimize the threshold current. The device structures will be modeled as a rectangular dielectric waveguide, with dielectric sidewalls and barrier materials on the top and bottom with dimensions engineered to maximize optical confinement.

The LD will follow a graded-index separate confinement heterostructure (GRINSCH) active design with the addition of an electron blocking layer. The multi-quantum well structure with its step-like two-dimensional density of states and quantized sub-bands reduce the threshold current required for stimulated emission and to improve the temperature stability. The light to current relationship will then be simulated with a varying number of wells (and thus threshold current). The carrier diffusion profile will determine the transverse gain profile, which will be designed to maximize the overlap with the laser profile. The final design (number, width, and composition of wells) will be tailored to the laser intensity and efficiency required.

6.2.2 Quantitative Investigation of Structure-Emission Correlation

By using a frequency tripled Ti:sapphire laser (266 nm) to optically create electron hole pairs in the c-GaN LD's active region, the behavior of carriers in the GRINSCH structure can be identified through the emission spectra. The initial experimental approach will include excitation dependent (from W/cm^2 to kW/cm^2) and temperature dependent (1.4 ~ 300 K) to identify the efficiency of carrier confinement in the quantum wells. Finally, temperature-dependent time-resolved emission spectroscopy will be used to quantify carrier recombination rate at different temperatures of the LD structures using a streak camera to achieve picosecond resolution. The carrier lifetime at different temperature can infer the fundamental recombination mechanisms (Shockley-Read-Hall, spontaneous radiative, or Auger) in the LD.

6.2.3 Fabrication of LDs

The fabrication of the LD will first involve optical lithography on thermally grown oxide on Si(100) substrate. Then anisotropic etching of the silicon substrate using potassium hydroxide (KOH) will be carried out, with etch time carefully chosen in accordance to Section 6.2.1. After the patterning is complete, material and device growth using MOCVD will be carried out, with an appropriate phase transition layer found in stage Section 6.2.1, and the DEVICE structures simulated in Section 6.2.2. To complete the packing of the device, deposition of passivation dielectric will be performed using plasma enhanced chemical vapor deposition (PECVD) and metal contacts using an electron beam evaporator.

6.2.4 Optoelectronic Characterization of c-GaN Devices Under Various Stresses

It is very important to test the stability and reliability of the LD under the various environment, such as outer space for space exploration applications. Three aspects are paramount to the success of a space-based UV laser: spectral stability, consistent lifetime, and mechanical robustness.

The spectral stability of the LD has to be characterized under a wide range of temperature that is typically seen on Mars and outer space, and then further remedied to ensure a tolerable range that could be corrected via laser cavity parameters. In addition to temperature, other harmful particles such as gamma rays, should be taken into consideration. The lifetime of the LD will be measured using heat induced accelerated aging to establish an expected working hour of the LD under full lasing output power. Mechanical tests to simulate the environment during takeoff, descend and/or landing of the spacecraft to verify the LD’s mechanical robustness will be carried out to ensure the LD assembly can survive these stresses to ensure it will be fully operational after deployment.

REFERENCES

[1] W.N. Carr and G.E. Pittman, Appl. Phys. Lett. **3**, 173 (1963).

[2] N. Holonyak and S.F. Bevacqua, Appl. Phys. Lett. **1**, 82 (1962).

[3] T.S. Perry, IEEE Spectr. **32**, 52 (1995).

[4] S. Nakamura, T. Mukai, and M. Senoh, Appl. Phys. Lett. **64**, 1687 (1994).

[5] P. Gorrotxategi, M. Consonni, and A. Gasse, J. Solid State Light. **2**, 1 (2015).

[6] J. Ueda, P. Dorenbos, A.J.J. Bos, A. Meijerink, and S. Tanabe, J. Phys. Chem. C **119**, 25003 (2015).

[7] M. Auf Der Maur, A. Pecchia, G. Penazzi, W. Rodrigues, and A. Di Carlo, Phys. Rev. Lett. **116**, 27401 (2016).

[8] K.A. Bulashevich, A. V. Kulik, and S.Y. Karpov, Phys. Status Solidi Appl. Mater. Sci. **212**, 914 (2015).

[9] D. Schiavon, M. Binder, M. Peter, B. Galler, P. Drechsel, and F. Scholz, Phys. Status Solidi Basic Res. **250**, 283 (2013).

[10] F.A.A.S.R. YUEWEI ZHANG, SRIRAM KRISHNAMOORTHY, Compd. Semicond. (2016).

[11] J. Piprek, Phys. Status Solidi Appl. Mater. Sci. **207**, 2217 (2010).

[12] G. Verzellesi, D. Saguatti, M. Meneghini, F. Bertazzi, M. Goano, G. Meneghesso, and E. Zanoni, J. Appl. Phys. **114**, 71101 (2013).

[13] J. Xie, X. Ni, Q. Fan, R. Shimada, Ü. Özgür, and H. Morkọ, Appl. Phys. Lett. **93**, 91 (2008).

[14] D.S. Meyaard, G.B. Lin, Q. Shan, J. Cho, E. Fred Schubert, H. Shim, M.H. Kim, and C. Sone, Appl. Phys. Lett. **99**, 1 (2011).

[15] M.H. Kim, M.F. Schubert, Q. Dai, J.K. Kim, E.F. Schubert, J. Piprek, and Y. Park, Appl. Phys. Lett. **91**, 1 (2007).

[16] Y.-S. Yoo, J.-H. Na, S.J. Son, and Y.-H. Cho, Sci. Rep. **6**, 34586 (2016).

[17] E. Kioupakis, P. Rinke, K.T. Delaney, and C.G. Van De Walle, Appl. Phys. Lett. **98**, 16 (2011).

[18] S. Hammersley, D. Watson-Parris, P. Dawson, M.J. Godfrey, T.J. Badcock, M.J. Kappers, C. McAleese, R.A. Oliver, and C.J. Humphreys, J. Appl. Phys. **111**, 83512 (2012).

[19] J. Hader, J. V. Moloney, and S.W. Koch, Appl. Phys. Lett. **96**, 221106 (2010).

[20] J. Piprek, Appl. Phys. Lett. **107**, 31101 (2015).

[21] W.C. Johnson and J.B. Parsons, J. Phys. Chem. **36**, 2588 (1931).

[22] H.P. Maruska and J.J. Tietjen, Appl. Phys. Lett. **15**, 327 (1969).

[23] H. Amano, N. Sawaki, I. Akasaki, and Y. Toyoda, Appl. Phys. Lett. **48**, 353 (1986).

[24] H. Amano, M. Kito, K. Hiramatsu, and I. Akasaki, Jpn. J. Appl. Phys. **28**, L2112 (1989).

[25] S. Nakamura, T. Mukai, M. Senoh, and N. Iwasa, Jpn. J. Appl. Phys. **31**, L139 (1992).

[26] R. Katayama, Matsuoka Lab Website (Www.matsuoka-Lab.imr.tohoku.ac.jp); Accessed 11 Oct 2017 (2012).

[27] I. Vurgaftman and J.R. Meyer, J. Appl. Phys. **94**, 3675 (2003).

[28] P. Schley, R. Goldhahn, A.T. Winzer, G. Gobsch, V. Cimalla, O. Ambacher, H. Lu, W.J. Schaff, M. Kurouchi, Y. Nanishi, M. Rakel, C. Cobet, and N. Esser, Phys. Rev. B - Condens. Matter Mater. Phys. **75**, 1 (2007).

[29] R. Liu and C. Bayram, J. Appl. Phys. **120**, 25106 (2016).

[30] B. Qu, X.H. Zheng, Y.T. Wang, D.P. Xu, S.M. Lin, H. Yang, and J.W. Liang, J. Cryst. Growth **227**, 399 (2001).

[31] M. Röppischer, R. Goldhahn, G. Rossbach, P. Schley, C. Cobet, N. Esser, T. Schupp, K. Lischka, and D.J. As, J. Appl. Phys. **106**, 1 (2009).

[32] P. Schley, R. Goldhahn, C. Napierala, G. Gobsch, J. Schörmann, D.J. As, K. Lischka, M. Feneberg, and K. Thonke, Semicond. Sci. Technol. **23**, 55001 (2008).

[33] S. Nakamura, M. Senoh, S. Nagahama, N. Iwasa, T. Yamada, T. Matsushita, H. Kiyoku, and Y. Sugimoto, Jpn. J. Appl. Phys. **35**, L217 (1996).

[34] D.G. Zhao, S.J. Xu, M.H. Xie, S.Y. Tong, and H. Yang, Appl. Phys. Lett. **83**, 677 (2003).

[35] J. Perozek, H.-P. Lee, B. Krishnan, A. Paranjpe, K.B. Reuter, D.K. Sadana, and C. Bayram, J. Phys. D. Appl. Phys. **50**, 55103 (2017).

[36] H. Morkoç, in *Handb. Nitride Semicond. Devices* (Wiley-VCH Verlag GmbH & Co. KGaA, 2009), pp. 1–129.

[37] F. Bernardini, V. Fiorentini, and D. Vanderbilt, Phys. Rev. B **56**, 4 (1997).

[38] S. Xu, Y. Hao, J. Zhang, T. Jiang, L. Yang, X. Lu, and Z. Lin, Nano Lett. **13**, 3654 (2013).

[39] Y. Zhao, Q. Yan, C.Y. Huang, S.C. Huang, P. Shan Hsu, S. Tanaka, C.C. Pan, Y. Kawaguchi, K. Fujito, C.G. Van De Walle, J.S. Speck, S.P. Denbaars, S. Nakamura, and D. Feezell, Appl. Phys. Lett. **100**, 0 (2012).

[40] S. Li, J. Schörmann, D.J. As, and K. Lischka, Appl. Phys. Lett. **90**, 10 (2007).

[41] J.G. Kim, A.C. Frenkel, H. Liu, and R.M. Park, Appl. Phys. Lett. **65**, 91 (1994).

[42] O. Brandt, H. Yang, H. Kostial, and K.H. Ploog, Appl. Phys. Lett. **69**, 2707 (1996).

[43] E.W.S. Caetano, R.N. Costa Filho, V.N. Freire, and J.A.P. Da Costa, Solid State Commun. **110**, 469 (1999).

[44] D.J. As, D. Schikora, A. Greiner, M. Lübbers, J. Mimkes, and K. Lischka, Phys. Rev. B **54**, R11118 (1996).

[45] K.T. Delaney, P. Rinke, and C.G. Van De Walle, Appl. Phys. Lett. **94**, 2007 (2009).

[46] C.-H. Kim and B.-H. Han, Solid State Commun. **106**, 127 (1998).

[47] S. Dhara, A. Datta, C.T. Wu, Z.H. Lan, K.H. Chen, Y.L. Wang, C.W. Hsu, C.H. Shen, L.C. Chen, and C.C. Chen, Appl. Phys. Lett. **84**, 5473 (2004).

[48] D.J. As, U. Köhler, M. Lübbers, J. Mimkes, and K. Lischka, Phys. Status Solidi Appl. Res. **188**, 699 (2001).

[49] S.F. Chichibu, T. Onuma, T. Aoyama, K. Nakajima, P. Ahmet, T. Chikyow, T. Sota, S.P. DenBaars, S. Nakamura, T. Kitamura, Y. Ishida, and H. Okumura, J. Vac. Sci. Technol. B Microelectron. Nanom. Struct. **21**, 1856 (2003).

[50] D. Ahn and S.H. Park, Japanese J. Appl. Physics, Part 1 Regul. Pap. Short Notes Rev. Pap. **35**, 6079 (1996).

[51] T. Kitamura, Y. Suzuki, Y. Ishida, X.Q. Shen, H. Nakanishi, S.F. Chichibu, and M. Shimizu, Phys. Status Solidi a-Applied Res. **188**, 705 (2001).

[52] B. Lv, Y. Tang, S. Lou, Y. Xu, and S. Zhou, J. Mater. Chem. C **4**, 5416 (2016).

[53] D.J. As, Microelectronics J. **40**, 204 (2009).

[54] R. Grady and C. Bayram, J. Phys. D. Appl. Phys. **50**, 265104 (2017).

[55] V.A. Chitta, J.A.H. Coaquira, J.R.L. Fernandez, C.A. Duarte, J.R. Leite, D. Schikora, D.J. As, K. Lischka, and E. Abramof, Appl. Phys. Lett. **85**, 3777 (2004).

[56] J.H. Buß, A. Schaefer, T. Schupp, D.J. As, D. Hägele, and J. Rudolph, Appl. Phys. Lett. **105**, (2014).

[57] S. Kako, M. Holmes, S. Sergent, M. B??rger, D.J. As, Y. Arakawa, M. Bürger, D.J. As, and Y. Arakawa, Appl. Phys. Lett. **104**, 2012 (2014).

[58] D.J. As, A. Richter, J. Busch, M. Lübbers, J. Mimkes, and K. Lischka, Phys. Status Solidi Appl. Res. **180**, 369 (2000).

[59] C.H. Wei, Z.Y. Xie, L.Y. Li, Q.M. Yu, and J.H. Edgar, J. Electron. Mater. **29**, 317 (2000).

[60] V.D. Compeán García, I.E.E. Orozco Hinostroza, A. Escobosa Echavarría, E. López Luna, A.G. Rodríguez, and M.A.A. Vidal, J. Cryst. Growth **418**, 120 (2015).

[61] Y. Cui, V.K. Lazorov, M.M. Goetz, H. Liu, D.P. Robertson, M. Gajdardziska-Josifovska, and L. Li, Appl. Phys. Lett. **82**, 4666 (2003).

[62] R.M. Kemper, M. Weinl, C. Mietze, M. Häberlen, T. Schupp, E. Tschumak, J.K.N. Lindner, K. Lischka, and D.J. As, J. Cryst. Growth **323**, 84 (2011).

[63] R.M. Kemper, M. Häberlen, T. Schupp, M. Weinl, M. Bürger, M. Ruth, C. Meier, T. Niendorf, H.J. Maier, K. Lischka, D.J. As, and J.K.N. Lindner, Phys. Status Solidi Curr. Top. Solid State Phys. **9**, 1028 (2012).

[64] K. Sato, M. Shikida, Y. Matsushima, T. Yamashiro, K. Asaumi, Y. Iriye, and M. Yamamoto, Sensors Actuators A Phys. **64**, 87 (1998).

[65] S.C. Lee, B. Pattada, S.D. Hersee, Y.B. Jiang, and S.R.J. Brueck, IEEE J. Quantum Electron. **41**, 596 (2005).

[66] S.C. Lee, N. Youngblood, Y.B. Jiang, E.J. Peterson, C.J.M. Stark, T. Detchprohm, C. Wetzel, and S.R.J. Brueck, Appl. Phys. Lett. **107**, 1 (2015).

[67] C. Bayram, J.A. Ott, K.-T.T. Shiu, C.-W.W. Cheng, Y. Zhu, J. Kim, M. Razeghi, and D.K. Sadana, Adv. Funct. Mater. **24**, 4492 (2014).

[68] C. Bayram, C.-W. Cheng, D.K. Sadana, and K.-T. Shiu, (2015).

[69] R. Liu and C. Bayram, Appl. Phys. Lett. **109**, 38 (2016).

[70] R. Liu and C. Bayram, US Pat. **62325659**, (2016).

[71] R. Liu, R. Schaller, C. Chen, and C. Bayram, ACS Photonics (2017).

[72] H. Siegle, L. Eckey, A. Hoffmann, C. Thomsen, B.K. Meyer, D. Schikora, M. Hankeln, and K. Lischka, Solid State Commun. **96**, 943 (1995).

[73] M.T. Durniak, A.S. Bross, D. Elsaesser, A. Chaudhuri, M.L. Smith, A.A. Allerman, S.C. Lee, S.R.J. Brueck, and C. Wetzel, Adv. Electron. Mater. 1 (2016).

[74] C. Bayram, K.T. Shiu, Y. Zhu, C.W. Cheng, D.K. Sadana, F.H. Teherani, D.J. Rogers, V.E. Sandana, P. Bove, Y. Zhang, S. Gautier, C.-Y. Cho, E. Cicek, Z. Vashaei, R. McClintock, and M. Razeghi, in *Proc. SPIE* (2013), p. 86260L.

[75] M. Athanasiou, R.M. Smith, S. Ghataora, and T. Wang, Sci. Rep. **7**, 39677 (2017).

[76] M. Feneberg, F. Lipski, R. Sauer, K. Thonke, P. Brückner, B. Neubert, T. Wunderer, and F. Scholz, J. Appl. Phys. **101**, 53530 (2007).

[77] Z. Zhuang, Y. Li, B. Liu, X. Guo, J. Dai, G. Zhang, T. Tao, T. Zhi, Z. Xie, H. Ge, Y. Shi, Y. Zheng, and R. Zhang, J. Appl. Phys. **118**, 233111 (2015).

[78] K.K. and S. Okayama, J. Phys. D. Appl. Phys. **5**, 43 (1972).

[79] M.A. Reshchikov, M. Zafar Iqbal, S.S. Park, K.Y. Lee, D. Tsvetkov, V. Dmitriev, and H. Morkoç, in *Phys. B Condens. Matter* (North-Holland, 2003), pp. 444–447.

[80] T. Azuhata, T. Sota, K. Suzuki, and S. Nakamura, J. Phys. Condens. Matter **7**, L129 (1995).

[81] J. Wu, H. Yaguchi, K. Onabe, R. Ito, and Y. Shiraki, Appl. Phys. Lett. **71**, 2067 (1997).

[82] C. Wang, D.J. As, B. Schöttker, D. Schikora, and K. Lischka, Semicond. Sci. Technol. **14**, 161 (1999).

[83] E. Glaser, J. Freitas, B. Shanabrook, D. Koleske, S. Lee, S. Park, and J. Han, Phys. Rev. B **68**, 0 (2003).

[84] D.J. As, F. Schmilgus, C. Wang, B. Schöttker, D. Schikora, and K. Lischka, Appl. Phys. Lett. **70**, 1311 (1997).

[85] H. Okumura, H. Hamaguchi, G. Feuillet, Y. Ishida, and S. Yoshida, Appl. Phys. Lett. **72**, 3056 (1998).

[86] J. Menniger, U. Jahn, O. Brandt, H. Yang, and K. Ploog, Appl. Phys. Lett. **69**, (1996).

[87] M.A. Reshchikov and H. Morkọ, J. Appl. Phys. **97**, (2005).

[88] R. Zhang and T.F. Kuech, Appl. Phys. Lett. **72**, 1611 (1998).

[89] Y.P. Varshni, Physica **34**, 149 (1967).

[90] R. Dingle, D.D. Sell, S.E. Stokowski, and M. Ilegems, Phys. Rev. B **4**, 1211 (1971).

[91] G. Ramírez-Flores, H. Navarro-Contreras, A. Lastras-Martínez, R.C. Powell, and J.E. Greene, Phys. Rev. B **50**, 8433 (1994).

[92] H. Teisseyre, P. Perlin, T. Suski, I. Grzegory, S. Porowski, J. Jun, A. Pietraszko, and T.D. Moustakas, J. Appl. Phys. **76**, (1994).

[93] W. Grieshaber, E.F. Schubert, I.D. Goepfert, R.F. Karlicek, M.J. Schurman, and C. Tran, J. Appl. Phys. **80**, 4615 (1996).

[94] J. Krustok, H. Collan, and K. Hjelt, J. Appl. Phys. **81**, 1442 (1997).

[95] Y. Narukawa, Y. Kawakami, S. Fujita, and S. Nakamura, Phys. Rev. B **59**, 10283 (1999).

[96] Y. Toyozawa, Prog. Theor. Phys. Suppl. **12**, 111 (1959).

[97] S. Hess, F. Walraet, R.A. Taylor, J.F. Ryan, B. Beaumont, and P. Gibart, Phys. Rev. B **58**, R15973 (1998).

[98] J. Simon, N.T. Pelekanos, C. Adelmann, E. Martinez-Guerrero, R. Andre, B. Daudin, L.S. Dang, and H. Mariette, Phys. Rev. B **68**, 35312 (2003).

[99] V.A. Fonoberov and A.A. Balandin, J. Appl. Phys. **94**, 7178 (2003).

[100] O. Marquardt, T. Hickel, and J. Neugebauer, J. Appl. Phys. **106**, (2009).

[101] S.F. Chichibu, H. Marchand, M.S. Minsky, S. Keller, P.T. Fini, J.P. Ibbetson, S.B. Fleischer, J.S. Speck, J.E. Bowers, E. Hu, U.K. Mishra, S.P. DenBaars, T. Deguchi, T. Sota, and S. Nakamura, Appl. Phys. Lett. **74**, 1460 (1999).

[102] H. Ki Kwon, C.. J. Eiting, D.J.. J.H. Lambert, M.. M. Wong, B.. S. Shelton, T.. G. Zhu, Z. Liliental-Weber, M. Benamura, and R.. D. Dupuis, J. Cryst. Growth **221**, 240 (2000).

[103] G.E. Bunea, W.D. Herzog, M.S. Unlu, B.B. Goldberg, and R.J. Molnar, Appl. Phys. Lett. **75**, 838 (1999).

[104] S.F. Chichibu, A. Uedono, T. Onuma, T. Sota, B.A. Haskell, S.P. Denbaars, J.S. Speck, and S. Nakamura, Appl. Phys. Lett. **86**, 21914 (2005).

[105] S.A. Church, S. Hammersley, P.W. Mitchell, M.J. Kappers, S.L. Sahonta, M. Frentrup, D. Nilsson, P.J. Ward, L.J. Shaw, D.J. Wallis, C.J. Humphreys, R.A. Oliver, D.J. Binks, and P. Dawson, Phys. Status Solidi **254**, 1600733 (2017).

APPENDIX A

INSTRUMENTS AND EQUIPMENT

A. 1 Scanning Electron Microscopy and Electron Backscatter Diffraction

The SEM images were taken on a JEOL 7000F field emission scanning electron microscope. The electron acceleration voltage used is 10 kV and the current is ~1 nA. The working distance is typically between 6 – 10 mm. Cross-sectional images were taken with the sample clamped on a “mini-vice” sample mount. Electron backscatter diffraction is also performed on this instrument. Oxford Instruments’ EBSD detector is mounted on the back of the SEM. Phase detection and analysis are done via Oxford Instruments’ (formerly known as HKL technology) EBSD analytical software *CHANNEL5*. An image of the SEM is shown in Figure 40. The EBSD detector is mounted on the back side of the SEM, as indicated by the red arrow.

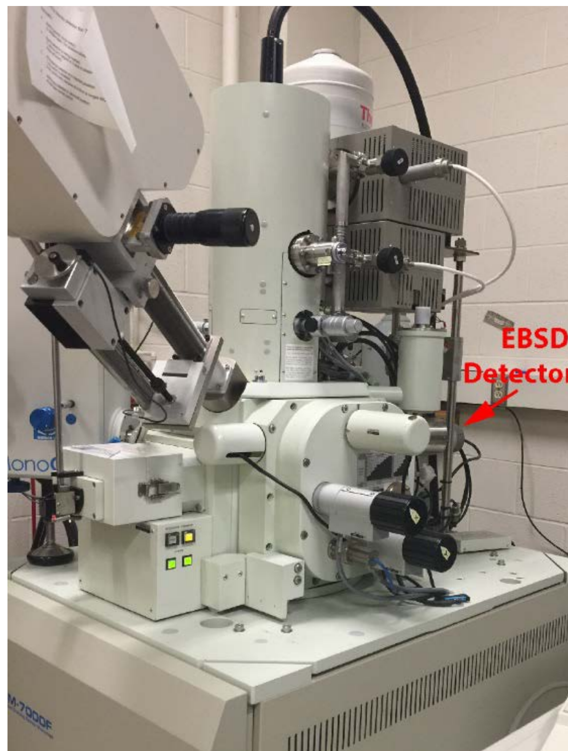

Figure 40 JEOL 7000F SEM with EBSD detector mounted on the back.

A. 2 Atomic Force Microscopy

The AFM study was conducted on an Asylum Cypher Atomic Force Microscope mounted on an optical table with continuous nitrogen flow supports. The tips used were BudgetSensors silicon AFM tips coated with aluminum (BS-Tap300Al). The system is capable of < 5 pm height resolution with a maximum lateral scan dimension of 30×30 µm and vertical maximum dimension of 5 µm. An image of the microscope is shown in Figure 41.

Figure 41 Asylum Cypher environmental AFM (image taken from manufacturer webpage at: asylumresearch.com/Products/Cypher/CypherProduct.shtml).

A. 3 Transmission Electron Microscopy

Transmission electron microscopy was conducted on a JEOL 2010 LaB_6 TEM attached with Gatan MatScan 1k×1k CCD and a DigitalMicrograph® computer control. The electron acceleration voltage is 200 kV, which yields a point resolution of 2.8Å. A cross-sectional piece of the U-grooves is taken out and thinned to ~50 nm by a focused ion beam (FEI Helios). An image of the TEM with the U-groove sample mounted and its image projected on the phosphor screen is shown in Figure 42.

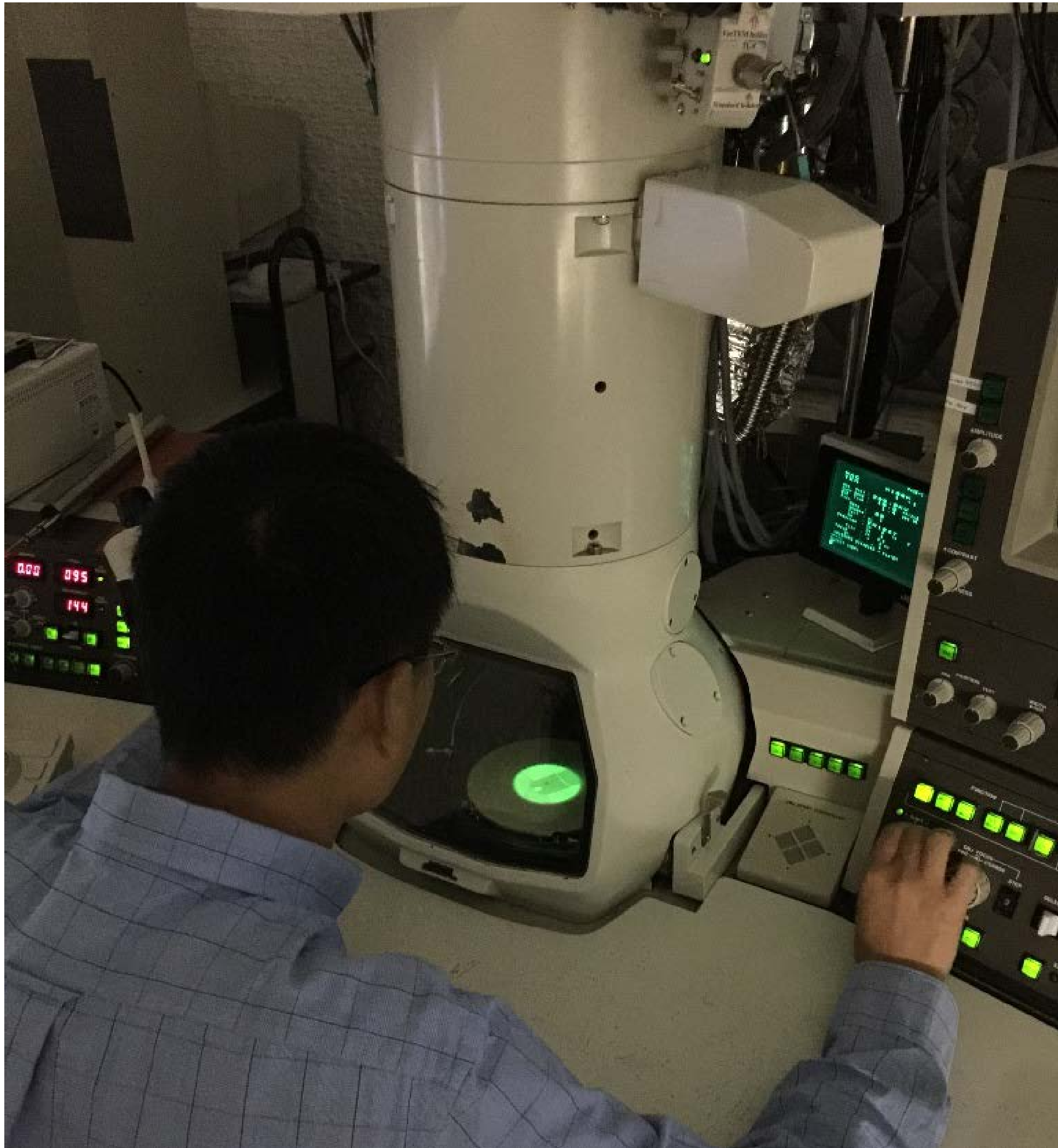

Figure 42 JEOL 2010 TEM with an U-groove image showing on the phosphor screen.

A. 4 Raman Spectroscopy

Raman spectroscopy was conducted on a Horiba LabRAM HR 3D confocal Raman imaging microscope with a 405 nm laser and a 100x, NA 0.95 objective lens. The signal was collected using a 1800 g/mm gratings blazed at 500 nm and a Horiba Synapse back-illuminated deep-depletion CCD camera.

Figure 43 Horiba Raman Confocal Imaging Microscope (image taken from UIUC Beckman Institute's website at: itg.beckman.illinois.edu/microscopy_suite/equipment/raman_imaging_system/).

A. 5 Cathodoluminescence

Cathodoluminescence was conducted on the same JEOL 7000F field emissions scanning electron microscope fitted with a Gatan MonoCL3 system. Signal collection was achieved using an imaging CCD (sensitive in the 300-900 nm range) with a 1200 g/mm grating blazed at 500 nm and a paraboloid mirror inserted in the specimen chamber. A liquid helium flow stage with heating coil is fitted for cryo-CL studies that is capable of temperature control range between 5.65 – 300 K. The instrument with its specimen chamber opened is shown in Figure 44. The brass-colored helium flow stage is seen being mounted in the specimen control stage. The spectrometer (Gatan MonoCL) with a CCD attached (brown) is mounted on the left of the SEM through a port opening for the insertion of the paraboloid mirror.

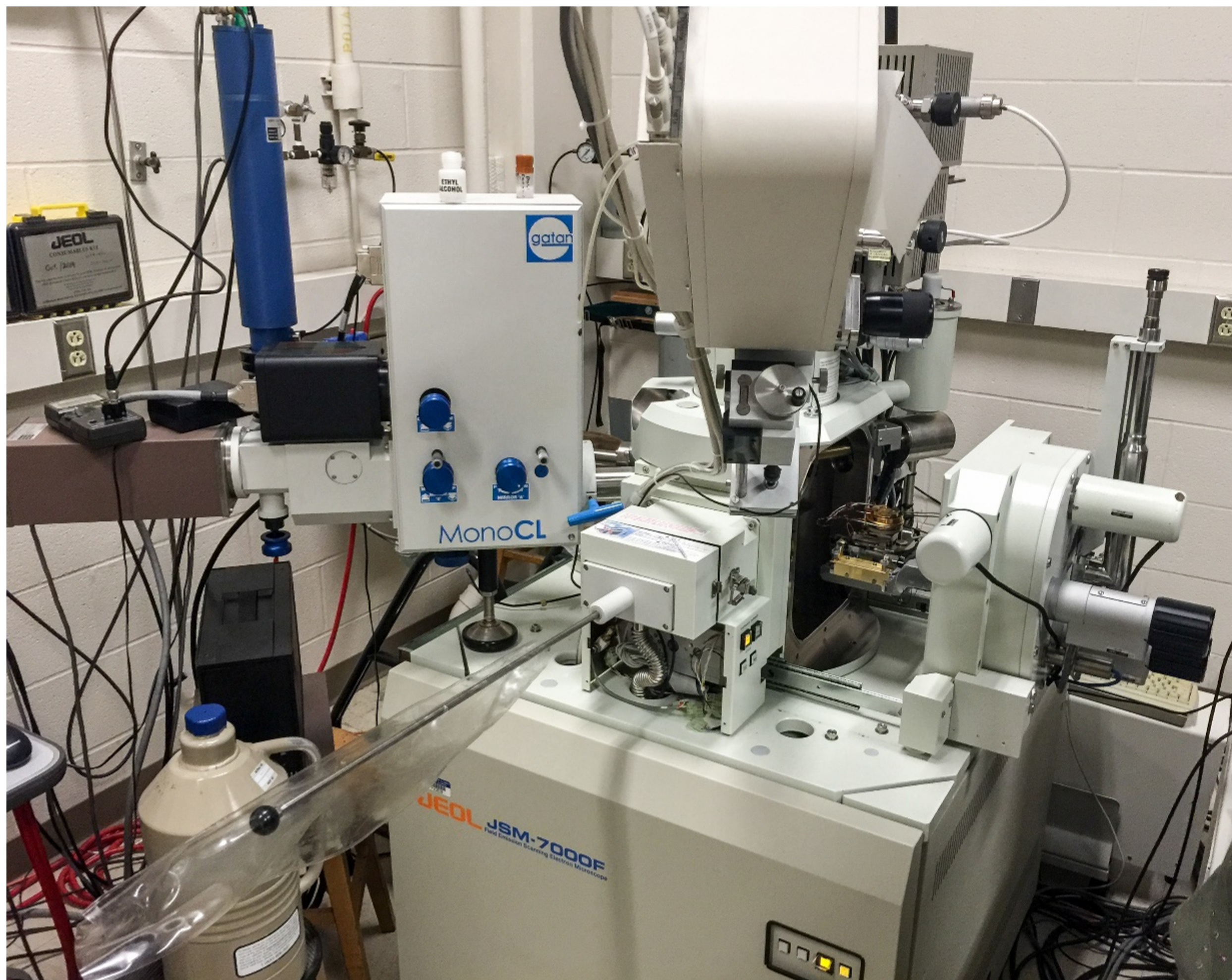

Figure 44 JEOL 7000F with Gatan MonoCL3 and cryogenic stage being fitted in the specimen chamber.

A. 6 Photoluminescence

Time-integrated photoluminescence and polarization-dependent PL were conducted using an unpolarized 266 nm continuous wave frequency-tripled Ti:Sapphire laser with an average output power of 10 mW with a UV-compatible wire grid polarizer fitting in front of a Princeton Instrument Acton SP-300i spectrometer using 1200l/mm grating blazed at 500 nm and a Princeton Instruments PIXIS high-performance CCD camera. The sample and luminescence collection optics are set up in a cardboard black box to isolate the CCD from stray light and potentially harmful scattered UV light. The PL setup outside and inside the black box is shown in Figure 45 and Figure 46, respectively.

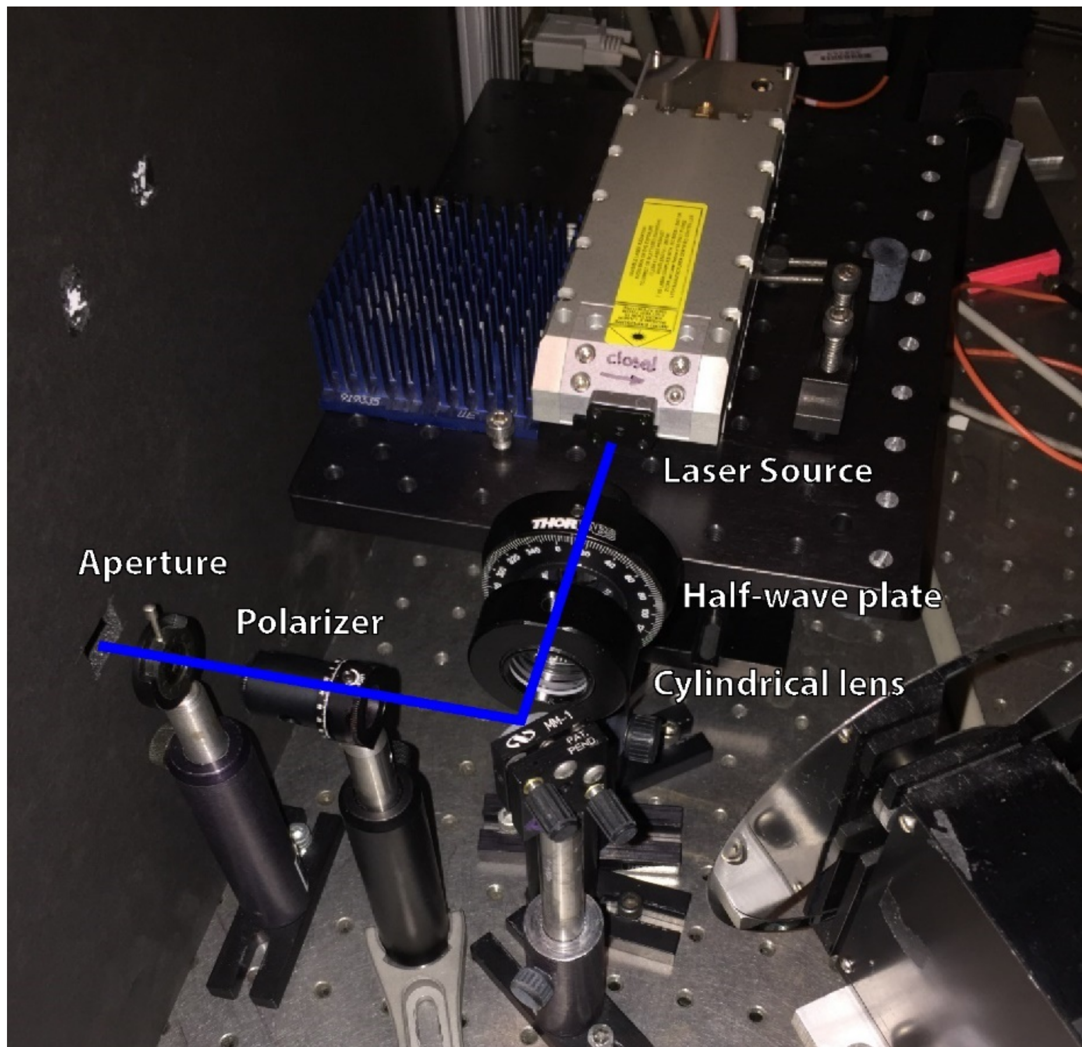

Figure 45 PL setup outside the black box with 266 nm laser showing in blue.

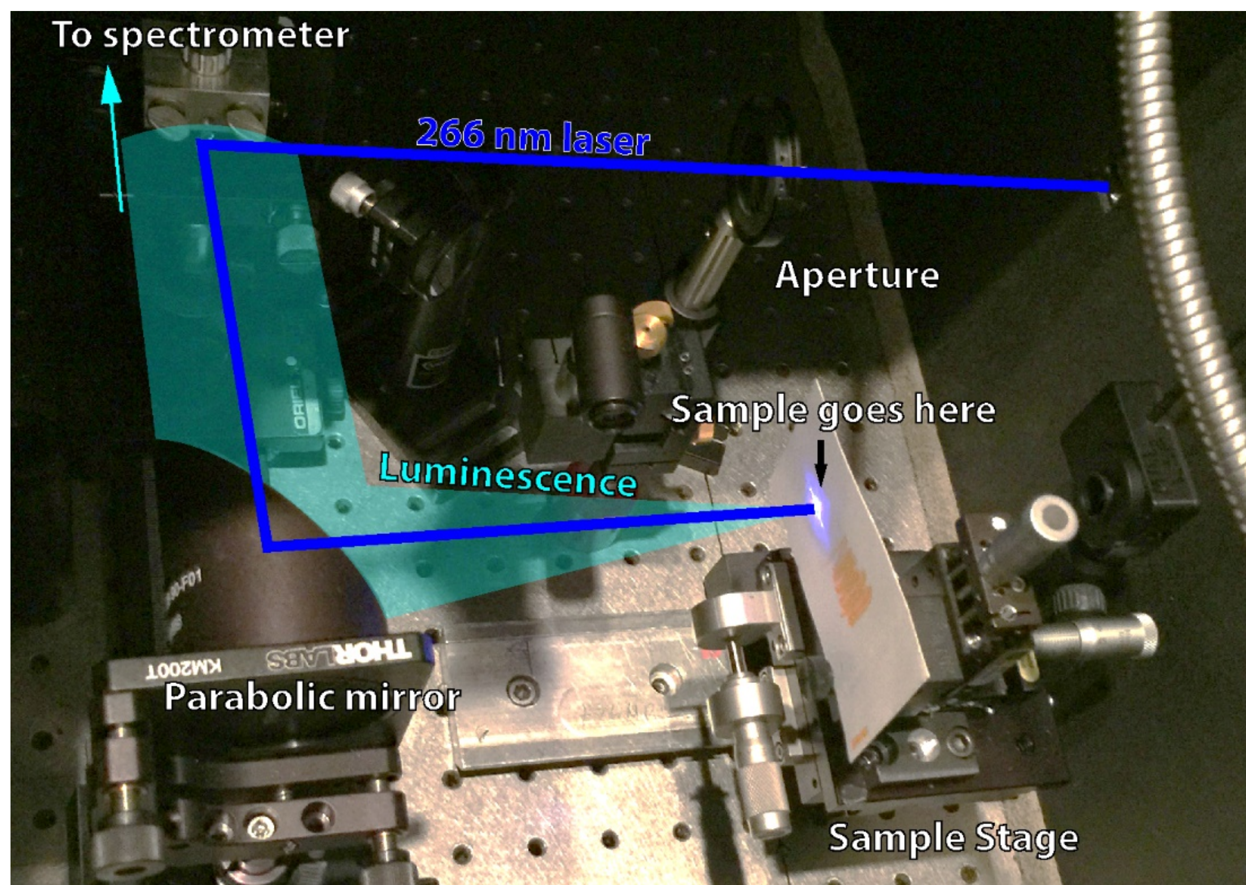

Figure 46 PL setup inside the black box showing laser beam in blue and sample luminescence in turquois.

A. 7 Time-Resolved Photoluminescence

Time-resolved photoluminescence study was conducted at Center for Nanoscale Materials at Argonne National Laboratory using a frequency-tripled Tsunami Ti:Sapphire pulsed laser with an average output power of ~ 5 mW with 100 fs pulses at 80 MHz. Signal was collected using a Hamamatsu streak camera system capable of < 1 ps resolution with a diffraction grating of 600 l/mm. Due to camera restrictions, no images of the facility was taken. An representative image of the TRPL setup taken from the website of Argonne National Laboratory is shown in Figure 47. A raw data image is shown in Figure 48.

Figure 47 Ultra-fast time-resolve photoluminescence setup at Center for Nanoscale Materials (image taken from ANL's website at: anl.gov/cnm/group/terahertz-ultraviolet-ultrafast-spectroscopy).

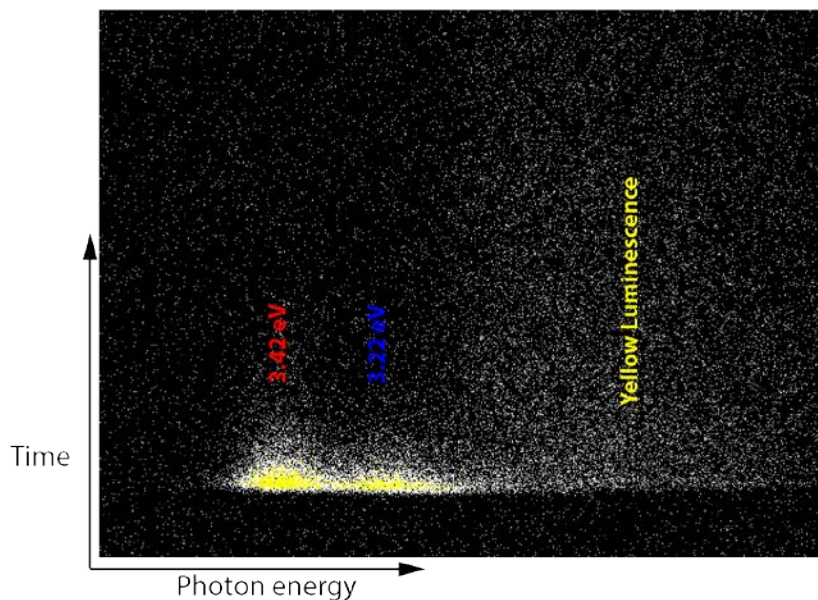

Figure 48 Streak camera data image. The left most photon cluster corresponds to the h-GaN emission (marked by red 3.42 eV). The middle cluster corresponds to c-GaN emission (blue 3.22 eV). The broad and slow-decaying photon cluster on the right is the defect yellow luminescence.